An arbitrary Lagrangian-Eulerian method for simulating interfacial dynamics between a hydrogel and a fluid

Lei Li [a,1], Jiaqi Zhang [b,1], Zelai Xu [a], Y.-N. Young [c], James J. Feng [a,d], Pengtao Yue [e,*]

[a] *Department of Chemical and Biological Engineering, University of British Columbia, Vancouver, BC V6T 1Z3, Canada*
[b] *School of Mathematical and Statistical Sciences, Clemson University, Clemson, SC 29634, USA*
[c] *Department of Mathematical Sciences, New Jersey Institute of Technology, Newark, NJ 07102, USA*
[d] *Department of Mathematics, University of British Columbia, Vancouver, BC V6T 1Z2, Canada*
[e] *Department of Mathematics, Virginia Tech, Blacksburg, VA 24061, USA*

A R T I C L E   I N F O

A B S T R A C T

Hydrogels are crosslinked polymer networks swollen with an aqueous solvent, and play central roles in biomicrofluidic devices. In such applications, the gel is often in contact with a flowing fluid, thus setting up a fluid-hydrogel two-phase system. Using a recently proposed model (Young et al. [41] 2019), we treat the hydrogel as a poroelastic material consisting of a Saint Venant-Kirchhoff polymer network and a Newtonian viscous solvent, and develop a finite-element method for computing flows involving a fluid-hydrogel interface. The interface is tracked by using a fixed-mesh arbitrary Lagrangian-Eulerian method that maps the interface to a reference configuration. The interfacial deformation is coupled with the fluid and solid governing equations into a monolithic algorithm using the finite-element library deal.II. The code is validated against available analytical solutions in several non-trivial flow problems: one-dimensional compression of a gel layer by a uniform flow, two-layer shear flow, and the deformation of a Darcy gel particle in a planar extensional flow. In all cases, the numerical solutions are in excellent agreement with the analytical solutions. Numerical tests show second-order convergence with respect to mesh refinement, and first-order convergence with respect to time-step refinement.

1. Introduction

Hydrogels are soft deformable materials containing a solid skeleton, usually an entangled polymer network, and an interstitial aqueous solvent. Because of their softness and lack of toxicity, hydrogels have found applications in many emerging technologies, e.g. in medical devices [1], drug delivery [2–5], tissue engineering [6,7] and stimulus-sensitive actuators [8–10]. Of particular note are recent developments of microfluidic devices that use hydrogel as scaffold or carrier for cell culture and drugs [11–16]. In such applications, gel-fluid two-phase flows play a central role. How does the exterior flow compress and deform the hydrogel surface through mechanical interactions? How does the fluid permeate the hydrogel, and how does

---

this permeation modify the structure and mechanical properties of the gel? Those questions have not been systematically examined before in the context of gel-fluid two-phase flows.

Previous studies of hydrogel mechanics fall into three categories. The first consists of solid-mechanics models that treat hydrogels as elastomers that swell due to solvent diffusion driven by the chemical potential of solvent-polymer interactions [17–19]. No fluid flow is involved. Besides, the swelling process is typically very slow, on the time scale of hours to days [20,21], and is essentially irrelevant to the flow situations of interest here.

The second category contains phenomenological yield-stress models such as the Bingham model [22,23]. These can be used to describe complex flow of viscoplastic fluids [24,25]. They treat the gel as a homogeneous material, with no regard to the constituent solvent and polymer chains. In this sense, therefore, they are one-phase instead of two-phase models. Nevertheless, in spatially nonuniform flows a portion of the gel may "yield" under stress to become fluid-like. Such a transition may create fluid and solid domains within the gel, and much effort has gone into the determination of the yield surface that evolves dynamically in complex flows [26,27]. Yielding does produce a two-phase flow situation, albeit in a different sense than the gel-solvent flow that is the focus of this study. We will not consider it further here.

The third category is the most relevant to the present work. Poroelastic models treat the gel as a mixture of two interpenetrating effective continua, one made of the solvent and the other of the polymer network [28]. Each component obeys its own mass and momentum balances, with interaction between the two phases. Despite its long history [29,30], this approach has so far seen limited applications in the fluid mechanics context. In most such applications, the gel-fluid interface is either immobile or has simple and easily computable displacements so as not to require the coupled solution of the fluid flow and elastic deformation of the solid skeleton. These include 1D shear flow past a layer of poroelastic material [31,32], 1D compression of a poroelastic layer [28], flow in a wavy channel coated with a thin poroelastic layer [33], and linear stability analysis of shear flow past a poroelastic layer [34–36]. Recently, poroelastic modeling has been used to explain the dynamics of the actomyosin gel inside biological cells [37,38].

At least two difficulties may have hindered the development of a two-phase poroelastic gel flow theory: the boundary conditions on the interface between the gel and the clear fluid, and the fluid-structure interaction problem in moving and deforming that interface. Note that we use the term "two-phase gel flow" to refer to the situation where a domain of gel coexists with a domain of pure fluid, separated by a dynamically deforming interface. A poroelastic model for the gel itself is sometimes called "two-phase" for the solvent and solid skeleton inside the gel [37]. The boundary condition between a porous medium and a clear fluid has long been a point of debate [39,40,32,41,42]. The crux is that an additional stress condition is needed because of the two momentum equations posed inside the gel for the network and interstitial fluid. The fluid-structure interaction problem on the gel interface is complicated by the fluid entering and exiting the solid network, making the "structure" a compressible and dynamically evolving entity.

Recently, Young et al. [41,42] took a new approach to these two difficulties. They invoked an energy dissipation argument to pose boundary conditions to ensure positive entropy production in the gel-fluid two-phase system. This led to velocity discontinuities at the interface, both between the gel and the exterior fluid and between the solid and solvent inside the gel, that are driven by stresses at the interface. Furthermore, Young et al. [41] applied such boundary conditions to solve the problem of a Darcy gel particle deforming slightly in an external flow field. The analytical solution was derived using perturbation in the limit of small deformations. This forms the starting point for the work to be presented here.

Our goal in the present paper is to construct a general computational method for gel-fluid two-phase flows. This is accomplished by overcoming the two obstacles discussed in the above. First, we develop a finite-element formalism to incorporate the complex and unconventional boundary conditions between a deforming hydrogel and an external fluid flow. Second, we develop a fixed-mesh arbitrary Lagrangian-Eulerian scheme to compute large deformations of the gel-fluid interface driven by the external flow.

2. Theoretical formulation

We adopt the poroelastic model for a fluid-permeated hydrogel as presented by Young et al. [41], together with recent developments of boundary conditions for the fluid-gel interface [42].

2.1. Governing equations

The computation domain Ω is divided into an inner region Ω_i occupied by the hydrogel and an outer region Ω_o occupied by the exterior viscous fluid (Fig. 1). The same fluid also permeates the pores of the hydrogel. Inside Ω_i, the fluid and solid phases are treated as interpenetrating continua, with volume fractions ϕ_f and ϕ_s that satisfy $\phi_f + \phi_s = 1$. The gel-fluid interface Γ is defined by the extent of the solid network or "skeleton" of the gel.

In Ω_o, the velocity $\mathbf{V}$ and the pressure P of the solvent satisfy the incompressible Stokes equations:

$$\nabla \cdot \mathbf{V} = 0, \tag{1}$$

$$\nabla \cdot (\boldsymbol{\Sigma} - P\mathbf{I}) = 0, \tag{2}$$

where $\boldsymbol{\Sigma} = \mu[\nabla \mathbf{V} + (\nabla \mathbf{V})^T]$ is the viscous stress tensor and μ is the solvent viscosity. We ignore fluid inertia as the target applications are typically microscopic slow flows. It will be straightforward to add inertia to the external flow.
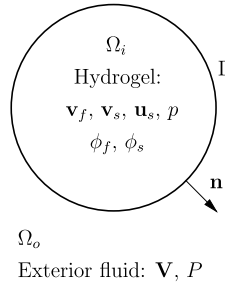
Fig. 1. A schematic of a particle of poroelastic gel in a Newtonian viscous fluid. The symbols are defined in the text.

In the hydrogel domain Ω_i, the volume conservation of each phase leads to the following continuity equations:

$$\frac{\partial \phi_f}{\partial t} + \nabla \cdot \left(\phi_f \mathbf{v}_f \right) = 0, \tag{3}$$

$$\frac{\partial \phi_s}{\partial t} + \nabla \cdot (\phi_s \mathbf{v}_s) = 0, \tag{4}$$

where $\mathbf{v}_f$ and $\mathbf{v}_s$ are, respectively, the *intrinsic phase-averaged* fluid and solid velocities [32], i.e. volume-averaged over a small volume that contains only one of the phases. The same average is implied for other gel-based quantities such as pressure and stress. Summing the two equations above gives us a solenoidal average velocity $\mathbf{q} = \phi_s \mathbf{v}_s + \phi_f \mathbf{v}_f$:

$$\nabla \cdot \left(\phi_s \mathbf{v}_s + \phi_f \mathbf{v}_f \right) = 0, \tag{5}$$

although neither $\mathbf{v}_f$ nor $\mathbf{v}_s$ is divergence-free in general.

Each phase satisfies a Brinkman-type momentum equation:

$$\nabla \cdot \left(\phi_f \boldsymbol{\sigma}_f \right) - \phi_f \nabla p + \mathcal{F}^{s \to f} = 0, \tag{6}$$

$$\nabla \cdot (\phi_s \boldsymbol{\sigma}_s) - \phi_s \nabla p + \mathcal{F}^{f \to s} = 0, \tag{7}$$

where $\boldsymbol{\sigma}_f$ and $\boldsymbol{\sigma}_s$ are the Cauchy stress tensors for the two phases, and p is the pressure in the hydrogel. The fluid stress is given by $\boldsymbol{\sigma}_f = \mu_e[\nabla \mathbf{v}_f + (\nabla \mathbf{v}_f)^T]$, where μ_e is the effective viscosity [42]. The solid stress $\boldsymbol{\sigma}_s$ is a function of the solid displacement $\mathbf{u}_s$, which is related to the solid velocity $\mathbf{v}_s$ by the kinematic equation

$$\frac{d\mathbf{u}_s}{dt} - \mathbf{v}_s = 0, \tag{8}$$

where $\frac{d}{dt} = \frac{\partial}{\partial t} + \mathbf{v}_s \cdot \nabla$ denotes the material derivative. For the solid stress tensor $\boldsymbol{\sigma}_s$, we adopt the Saint Venant-Kirchhoff constitutive model. Since the strain and stress tensors need to be posed in the Lagrangian frame, we defer the equations to Sec. 4.2, after describing the Lagrangian-Eulerian transformation. The frictional force or Darcy drag between the skeleton and the solvent is given by

$$\mathcal{F}^{s \to f} = -\mathcal{F}^{f \to s} = \xi \phi_f \phi_s \left(\mathbf{v}_s - \mathbf{v}_f \right), \tag{9}$$

where the drag coefficient ξ is taken to be a constant.

2.2. Boundary conditions

The boundary conditions (BCs) between a clear fluid and a porous medium have long been a subject of investigation and debate [39,43,44,40,45,32]. The root of the difficulty is that with a homogenized view of the porous medium as a mixture of fluid and solid, any geometric information of the fluid-fluid and fluid-solid contact at the nominal interface is lost. Should the fluid velocity be continuous across the interface? How should the traction from the pure fluid side be sustained by the fluid and solid components on the porous side? Moreover, these questions are sometimes obscured by the use of different volume averaging schemes [32].

Recently, Young et al. [41,42] took a thermodynamically based approach to the question of the BCs on a fluid-gel interface. First, the fluid mass balance and total traction balance on the interface Γ yield two generally valid BCs:

$$(\mathbf{V} - \mathbf{v}_s) \cdot \mathbf{n} = \phi_f \left(\mathbf{v}_f - \mathbf{v}_s \right) \cdot \mathbf{n}, \tag{10}$$

$$\left(-p\mathbf{I} + \phi_f \boldsymbol{\sigma}_f + \phi_s \boldsymbol{\sigma}_s \right) \cdot \mathbf{n} = (-P\mathbf{I} + \boldsymbol{\Sigma}) \cdot \mathbf{n}. \tag{11}$$

Next, the principle of energy dissipation suggests relations between the velocity jumps at the interface and the tractions on either side of the interface. Such a proposal being sufficient but non-unique for guaranteeing positive entropy production on Γ, two sets of BCs have been postulated to supplement Eqs. (10), (11):

$$
\text{BC1}: \begin{cases}
(\mathbf{V} - \mathbf{v}_s) \cdot \mathbf{n} = \eta\, \mathbf{n} \cdot [(\boldsymbol{\Sigma} - P\mathbf{I}) - (\boldsymbol{\sigma}_f - p\mathbf{I})] \cdot \mathbf{n}, \\
(\mathbf{V} - \mathbf{v}_s) \cdot \mathbf{T} = \beta\, (\boldsymbol{\Sigma} \cdot \mathbf{n}) \cdot \mathbf{T}, \\
\phi_f (\mathbf{v}_f - \mathbf{v}_s) \cdot \mathbf{T} = -\beta\, (\boldsymbol{\sigma}_f \cdot \mathbf{n}) \cdot \mathbf{T},
\end{cases}
\tag{12}
$$

$$
\text{BC2}: \begin{cases}
(\mathbf{V} - \mathbf{v}_f) \cdot \mathbf{n} = \eta\, \mathbf{n} \cdot [(\boldsymbol{\Sigma} - P\mathbf{I}) - (\boldsymbol{\sigma}_s - p\mathbf{I})] \cdot \mathbf{n}, \\
(\mathbf{V} - \mathbf{v}_f) \cdot \mathbf{T} = \beta\, (\boldsymbol{\Sigma} \cdot \mathbf{n}) \cdot \mathbf{T}, \\
\phi_s (\mathbf{v}_s - \mathbf{v}_f) \cdot \mathbf{T} = -\beta\, (\boldsymbol{\sigma}_s \cdot \mathbf{n}) \cdot \mathbf{T},
\end{cases}
\tag{13}
$$

where $\eta > 0$ is an interfacial permeability, $\beta > 0$ is an interfacial slip coefficient, $\mathbf{n}$ is the unit normal pointing from Ω_i to Ω_o, and $\mathbf{T} = \mathbf{I} - \mathbf{n} \otimes \mathbf{n}$ is the projection tensor that projects vectors to the tangent plane of Γ.

For the purpose of this paper, we will adopt BC1 as the default. An exception is the two-layer shear flow of Sec. 5.2, where a comparison with BC2 is made. Questions remain, of course, regarding which more faithfully represents real flow situations. These will be investigated further in separate studies.

3. Finite-element weak form

A unique feature of the weak form is the incorporation of the boundary conditions of Eqs. (10)–(12). We solve the governing equations by the Galerkin finite element method. In particular, we seek weak solutions $\mathbf{V} \in H^1(\Omega_o)$, $P \in L^2(\Omega_o)$, $\mathbf{v}_f \in H^1(\Omega_i)^d$, $\mathbf{v}_s \in H^1(\Omega_i)^d$, $\mathbf{u}_s \in H^1(\Omega_i)^d$, $p \in L^2(\Omega_i)$, and $\phi_s \in L^2(\Omega_i)$, where d is the spatial dimension of the problem. The corresponding test functions are $\Psi_{\mathbf{V}}$, Ψ_P, $\Psi_{\mathbf{v}_f}$, $\Psi_{\mathbf{v}_s}$, $\Psi_{\mathbf{u}_s}$, Ψ_p, and Ψ_{ϕ_s}, respectively. ϕ_f can be directly computed from $\phi_f = 1 - \phi_s$.

The weak formulations of Eqs. (1), (2), (5)–(7) can be obtained by taking the inner products of Eq. (1) with Ψ_P in Ω_o, Eq. (2) with $\Psi_{\mathbf{V}}$ in Ω_o, Eq. (5) with Ψ_p in Ω_i, Eq. (6) with $\Psi_{\mathbf{v}_f}$ in Ω_i, and Eq. (7) with $\Psi_{\mathbf{v}_s}$ in Ω_i. By summing up these inner products, performing integration by parts, and plugging in Eq. (12), we arrive at the unified weak form for BC1:

$$
\begin{aligned}
& (\boldsymbol{\Sigma}, \nabla \Psi_{\mathbf{V}})_{\Omega_o} - ((\boldsymbol{\Sigma} - P\mathbf{I}) \cdot \mathbf{n}, \Psi_{\mathbf{V}})_{\partial\Omega_o \backslash \Gamma} \\
& + \left(\phi_f \boldsymbol{\sigma}_f, \nabla \Psi_{\mathbf{v}_f}\right)_{\Omega_i} - \left(\phi_f (\boldsymbol{\sigma}_f - p\mathbf{I}) \cdot \mathbf{n}, \Psi_{\mathbf{v}_f}\right)_{\partial\Omega_i \backslash \Gamma} \\
& + \left(\phi_s \boldsymbol{\sigma}_s, \nabla \Psi_{\mathbf{v}_s}\right)_{\Omega_i} - \left(\phi_s (\boldsymbol{\sigma}_s - p\mathbf{I}) \cdot \mathbf{n}, \Psi_{\mathbf{v}_s}\right)_{\partial\Omega_i \backslash \Gamma} \\
& - (P, \nabla \cdot \Psi_{\mathbf{V}})_{\Omega_o} + (\nabla \cdot \mathbf{V}, \Psi_P)_{\Omega_o} \\
& - \left(p, \nabla \cdot (\phi_f \Psi_{\mathbf{v}_f} + \phi_s \Psi_{\mathbf{v}_s})\right)_{\Omega_i} + \left(\nabla \cdot (\phi_f \mathbf{v}_f + \phi_s \mathbf{v}_s), \Psi_p\right)_{\Omega_i} \\
& + \left(\xi \phi_f \phi_s (\mathbf{v}_f - \mathbf{v}_s), \Psi_{\mathbf{v}_f} - \Psi_{\mathbf{v}_s}\right)_{\Omega_i} + \left(\frac{1}{\eta}(\mathbf{V} - \mathbf{v}_s) \cdot \mathbf{n}, (\Psi_{\mathbf{V}} - \Psi_{\mathbf{v}_s}) \cdot \mathbf{n}\right)_{\Gamma} \\
& + \left(\frac{1}{\beta}(\mathbf{V} - \mathbf{v}_s) \cdot \mathbf{T}, \Psi_{\mathbf{V}} - \Psi_{\mathbf{v}_s}\right)_{\Gamma} + \left(\frac{\phi_f^2}{\beta}(\mathbf{v}_f - \mathbf{v}_s) \cdot \mathbf{T}, \Psi_{\mathbf{v}_f} - \Psi_{\mathbf{v}_s}\right)_{\Gamma} \\
& = 0,
\end{aligned}
\tag{14}
$$

where $(\cdot, \cdot)$ denotes the inner product over the region specified by the subscript. Here, the outer boundary $\partial\Omega$ is partitioned into $\partial\Omega_o \backslash \Gamma$ and $\partial\Omega_i \backslash \Gamma$: $\partial\Omega_o \backslash \Gamma$ is a segment of the outer boundary not in contact with the gel, and $\partial\Omega_i \backslash \Gamma$ is part of the gel surface not in contact with the exterior fluid but with, say, a solid wall.

The above formulation is notable for the treatment of the boundary conditions (Eqs. (10)–(12)). First, we have used Eq. (10) as an essential condition and thus the test functions for velocities satisfy the same constraint:

$$
(\Psi_{\mathbf{V}} - \Psi_{\mathbf{v}_s})\big|_{\Gamma} \cdot \mathbf{n} = \phi_f (\Psi_{\mathbf{v}_f} - \Psi_{\mathbf{v}_s})\big|_{\Gamma} \cdot \mathbf{n}.
\tag{15}
$$

Then, the traction balance of Eq. (11) and the velocity jumps of Eqs. (12) are incorporated into the boundary integrals. It is remarkable that the surface integrals on Γ can be combined into such simple forms. Detailed derivation can be found in Appendix A.

The weak formulations of Eqs. (4) and (8) are straightforward:

$$
\left(\frac{\partial \phi_s}{\partial t} + \nabla \cdot (\phi_s \mathbf{v}_s), \Psi_{\phi_s}\right)_{\Omega_i} = 0,
\tag{16}
$$

$$
\left(\frac{d\mathbf{u}_s}{dt} - \mathbf{v}_s, \Psi_{\mathbf{u}_s}\right)_{\Omega_i} = 0.
\tag{17}
$$

We keep these two equations separate from Eq. (14) because combining them does not lead to a simpler formulation. Besides, these two equations involve time derivatives and need to be solved by a time-stepping scheme while Eq. (14) evolves accordingly in a quasi-static fashion.

By taking $\Psi_{\mathbf{V}} = \mathbf{V}$, $\Psi_{\mathbf{v}_f} = \mathbf{v}_f$, $\Psi_{\mathbf{v}_s} = \mathbf{v}_s$, $\Psi_P = P$, and $\Psi_p = p$, Eq. (14) yields

$$
\begin{aligned}
\int_{\Omega_i} \phi_s \boldsymbol{\sigma}_s : \nabla \mathbf{v}_s d\mathbf{x} =& \int_{\partial\Omega_o \backslash \Gamma} \mathbf{V} \cdot (\boldsymbol{\Sigma} - P\mathbf{I}) \cdot \mathbf{n} ds \\
&+ \int_{\partial\Omega_i \backslash \Gamma} \phi_f \mathbf{v}_f \cdot (\boldsymbol{\sigma}_f - p\mathbf{I}) \cdot \mathbf{n} ds + \int_{\partial\Omega_i \backslash \Gamma} \phi_s \mathbf{v}_s \cdot (\boldsymbol{\sigma}_s - p\mathbf{I}) \cdot \mathbf{n} ds \\
&- \int_{\Omega_o} \boldsymbol{\Sigma} : \nabla \mathbf{V} d\mathbf{x} - \int_{\Omega_i} \phi_f \boldsymbol{\sigma}_f : \nabla \mathbf{v}_f d\mathbf{x} \\
&- \int_{\Omega_i} \xi \phi_f \phi_s |\mathbf{v}_f - \mathbf{v}_s|^2 d\mathbf{x} \\
&- \int_{\Gamma} \left[((\mathbf{V} - \mathbf{v}_s) \cdot \mathbf{n})^2 + \frac{1}{\beta} |(\mathbf{V} - \mathbf{v}_s) \cdot \mathbf{T}|^2 + \frac{\phi_f^2}{\beta} |(\mathbf{v}_f - \mathbf{v}_s) \cdot \mathbf{T}|^2 \right] ds,
\end{aligned}
\tag{18}
$$

which is exactly the same dissipative energy law as Eq. (21) in [41]. For a hyperelastic skeleton, the left-hand side can be expressed as $\frac{d\mathcal{E}}{dt}$, where $\mathcal{E}$ is the elastic energy stored in the solid skeleton [41,46]. On the right-hand side, the terms on the first and second lines are the external work done on the outer boundary. The terms in the third line are viscous dissipations of fluids outside and inside the hydrogel, respectively. The fourth line is the dissipation due to the Darcy drag between the solid and fluid phases inside the hydrogel. The terms in the last line are dissipations due to boundary conditions on the hydrogel interface. All these dissipation terms are non-positive, which guarantees that the free energy of the whole system (i.e., $\mathcal{E}$) decreases in time if there is no external work. Physically, this dissipative energy law ensures the model's consistency with the second law of thermal dynamics. Numerically, it plays an important role in the stability of solutions and may guide the design of energy-stable numerical schemes [47].

Different boundary conditions on hydrogel interface will lead to different inner product terms on Γ in Eq. (14). To use BC2 of Eq. (13) in place of BC1, we only need to replace the terms

$$
\left(\frac{1}{\eta} (\mathbf{V} - \mathbf{v}_s) \cdot \mathbf{n}, (\Psi_{\mathbf{V}} - \Psi_{\mathbf{v}_s}) \cdot \mathbf{n} \right)_{\Gamma} + \left(\frac{1}{\beta} (\mathbf{V} - \mathbf{v}_s) \cdot \mathbf{T}, \Psi_{\mathbf{V}} - \Psi_{\mathbf{v}_s} \right)_{\Gamma}
$$

with

$$
\left(\frac{1}{\eta} (\mathbf{V} - \mathbf{v}_f) \cdot \mathbf{n}, (\Psi_{\mathbf{V}} - \Psi_{\mathbf{v}_f}) \cdot \mathbf{n} \right)_{\Gamma} + \left(\frac{1}{\beta} (\mathbf{V} - \mathbf{v}_f) \cdot \mathbf{T}, \Psi_{\mathbf{V}} - \Psi_{\mathbf{v}_f} \right)_{\Gamma}
$$

in the weak form of Eq. (14). Thanks to their thermodynamic basis, both formulations lead to an energy law in the finite-element representations. In contrast, ad hoc BCs, say based on stress partition [31,32], would not allow simplifications of the surface integrals in the weak form, and would not lead to an energy law.

4. Fixed-mesh ALE method

To handle the interfacial deformation, we adopt an arbitrary Lagrangian-Eulerian (ALE) method. The ALE method can be implemented by two different approaches: to use a fixed mesh and a formulation in the reference frame, or to use a moving mesh and a formulation in the Eulerian frame [48]. Theoretically, these two approaches are equivalent. Although the Eulerian formulation is algebraically simpler than the reference-frame formulation, the moving mesh is more challenging to work with than the fixed mesh. We thus choose the fixed-mesh ALE approach in this work.

4.1. ALE mapping

In essence, we use a coordinate transformation to map the deformed domain to a time-independent reference domain, and solve the transformed governing equations in the latter. In the following, we use the hat $\hat{}$ to mark quantities defined in the reference frame. We introduce a reference frame with coordinates $\hat{\mathbf{x}}$ that coincides with $\mathbf{x}$ at the initial time t_0. We further define the reference domains $\hat{\Omega}$, $\hat{\Omega}_o$ and $\hat{\Omega}_i$ to be time-independent and overlapping the initial physical domains Ω, Ω_o, and Ω_i, respectively. The displacement field $\hat{\mathbf{u}}(\hat{\mathbf{x}}, t)$ defines an invertible mapping $\mathcal{M}_t$ from the reference domain to the physical domain at time t: $\mathcal{M}_t : \hat{\Omega} \to \Omega(t), \hat{\mathbf{x}} \mapsto \mathbf{x} = \hat{\mathbf{x}} + \hat{\mathbf{u}}(\hat{\mathbf{x}}, t)$. Every field function $f(\mathbf{x}, t)$ can thus be redefined in the reference frame as $\hat{f}(\hat{\mathbf{x}}, t) := f(\mathbf{x}(\hat{\mathbf{x}}, t), t)$.

In $\hat{\Omega}_i$ occupied by the elastic solid, it is customary to choose $\hat{\mathbf{u}} = \hat{\mathbf{u}}_s$ such that the reference frame reduces to the Lagrangian frame. The displacement field can be extended to $\hat{\mathbf{u}} = \hat{\mathbf{u}}_f$ in $\hat{\Omega}_o$ by different techniques, such as harmonic extension, biharmonic extension, and pseudo-elasticity extension, to reduce the distortion of the mapping $\mathcal{M}_t$ [48]. In this work, for simplicity, we choose the harmonic extension with a stiffening parameter α:

$$\frac{\partial \hat{\mathbf{u}}_s}{\partial t} - \hat{\mathbf{v}}_s = 0 \quad \text{in } \hat{\Omega}_i \tag{19}$$

and

$$\hat{\nabla} \cdot (\alpha \hat{\nabla} \hat{\mathbf{u}}_f) = 0 \quad \text{in } \hat{\Omega}_o \tag{20}$$

with the Dirichlet condition $\hat{\mathbf{u}}_f = \hat{\mathbf{u}}_s$ on $\hat{\Gamma}$ and the no-slip ($\hat{\mathbf{u}}_f = 0$) or slip condition on $\partial\hat{\Omega}_o \backslash \hat{\Gamma}$. The slip condition can be expressed as $(\hat{\mathbf{n}} \cdot \hat{\nabla})\hat{u}_{f\parallel} = 0$ and $\hat{u}_{f\perp} = 0$, where $\hat{u}_{f\parallel}$ and $\hat{u}_{f\perp}$ are the tangential and normal components of $\hat{\mathbf{u}}_f$, respectively. Often, the slip condition is preferred because it leads to a smaller distortion in $\hat{\mathbf{u}}_f$. It should be noted that the material derivative $\frac{d\mathbf{u}_s}{dt}$ reduces to $\frac{\partial \hat{\mathbf{u}}_s}{\partial t}$ in the reference frame. Since $\hat{\mathbf{u}}_s$ and $\hat{\mathbf{u}}_f$ are continuous across $\hat{\Gamma}$, the two equations above can be solved together using a single function $\hat{\mathbf{u}}$ in the continuous finite element space defined on $\hat{\Omega}$.

Based on the displacement field we can define the deformation gradient tensor

$$\hat{\mathbf{F}} := \frac{\partial \mathbf{x}}{\partial \hat{\mathbf{x}}} = \mathbf{I} + \hat{\nabla}\hat{\mathbf{u}} \tag{21}$$

and its determinant $\hat{J} := \det(\hat{\mathbf{F}})$. Correspondingly, we define $\mathbf{F} := \frac{\partial \hat{\mathbf{x}}}{\partial \mathbf{x}} = \hat{\mathbf{F}}^{-1}$ and $J := \det(\mathbf{F}) = \hat{J}^{-1}$ for the inverse mapping from $\mathbf{x}$ to $\hat{\mathbf{x}}$. In this work, we use the convention $(\nabla\mathbf{w})_{ij} = \left(\frac{\partial\mathbf{w}}{\partial\mathbf{x}}\right)_{ij} = \frac{\partial w_i}{\partial x_j}$ and $(\nabla\cdot\mathbf{W})_i = \frac{\partial W_{ij}}{\partial x_j}$. For any scalar field f, vector field $\mathbf{w}$, and tensor field $\mathbf{W}$, the derivatives in the two different frames are connected by the following relations: $\nabla f = \hat{\nabla}\hat{f} \cdot \hat{\mathbf{F}}^{-1}$, $\nabla\mathbf{w} = \hat{\nabla}\hat{\mathbf{w}} \cdot \hat{\mathbf{F}}^{-1}$, $\nabla\cdot\mathbf{w} = \hat{\nabla}\hat{\mathbf{w}} : \hat{\mathbf{F}}^{-T}$, and $\nabla\cdot\mathbf{W} = \hat{\nabla}\hat{\mathbf{W}} : \hat{\mathbf{F}}^{-T}$. The volume integrals satisfy $\int_\Omega f d\mathbf{x} = \int_{\hat{\Omega}} \hat{f}\hat{J}d\hat{\mathbf{x}}$.

4.2. Constitutive model for the skeleton

For the constitutive equation of the solid phase in the hydrogel, we choose the hyperelastic Saint Venant-Kirchhoff model, which allows large deformation. In $\hat{\Omega}_i$, we define the Green-Lagrange strain tensor

$$\hat{\mathbf{E}} = \frac{1}{2}(\hat{\mathbf{F}}^T \cdot \hat{\mathbf{F}} - \mathbf{I}) = \frac{1}{2}\left[\hat{\nabla}\hat{\mathbf{u}} + (\hat{\nabla}\hat{\mathbf{u}})^T + (\hat{\nabla}\hat{\mathbf{u}})^T \cdot (\hat{\nabla}\hat{\mathbf{u}})\right]. \tag{22}$$

The second Piola-Kirchhoff stress tensor is given by

$$\hat{\mathbf{S}} = 2\mu_s\hat{\mathbf{E}} + \lambda_s \text{tr}(\hat{\mathbf{E}})\mathbf{I}, \tag{23}$$

where λ_s and μ_s are the Lamé constants of the solid skeleton. The Cauchy stress tensor can then be obtained from

$$\hat{\boldsymbol{\sigma}}_s = \frac{1}{\hat{J}}\hat{\mathbf{F}} \cdot \hat{\mathbf{S}} \cdot \hat{\mathbf{F}}^T. \tag{24}$$

This enters the momentum balance of the solid skeleton, as in the weak form given below.

4.3. Weak form in the reference frame

In the reference frame, we seek weak solutions $\hat{\mathbf{V}} \in H^1(\hat{\Omega}_o)$, $\hat{P} \in L^2(\hat{\Omega}_o)$, $\hat{\mathbf{v}}_f \in H^1(\hat{\Omega}_i)^d$, $\hat{\mathbf{v}}_s \in H^1(\hat{\Omega}_i)^d$, $\hat{p} \in L^2(\hat{\Omega}_i)$, and $\hat{\phi}_s \in L^2(\hat{\Omega}_i)$, with the corresponding test functions $\hat{\Psi}_{\mathbf{V}}$, $\hat{\Psi}_P$, $\hat{\Psi}_{\mathbf{v}_f}$, $\hat{\Psi}_{\mathbf{v}_s}$, $\hat{\Psi}_p$, and $\hat{\Psi}_{\phi_s}$. The weak form of Eq. (14) is then transformed to

$$\left(\hat{J}\hat{\boldsymbol{\Sigma}} \cdot \hat{\mathbf{F}}^{-T}, \hat{\nabla}\hat{\Psi}_{\mathbf{V}}\right)_{\hat{\Omega}_o} - \left([\hat{J}(\hat{\boldsymbol{\Sigma}} - \hat{P}\mathbf{I}) \cdot \hat{\mathbf{F}}^{-T}] \cdot \hat{\mathbf{n}}, \Psi_{\mathbf{V}}\right)_{\partial\hat{\Omega}_o\backslash\hat{\Gamma}}$$

$$+ \left(\hat{\phi}_f(\hat{J}\hat{\boldsymbol{\sigma}}_f \cdot \hat{\mathbf{F}}^{-T}), \hat{\nabla}\hat{\Psi}_{\mathbf{v}_f}\right)_{\hat{\Omega}_i} - \left(\hat{\phi}_f[\hat{J}(\hat{\boldsymbol{\sigma}}_f - \hat{p}\mathbf{I}) \cdot \hat{\mathbf{F}}^{-T}] \cdot \hat{\mathbf{n}}, \hat{\Psi}_{\mathbf{v}_f}\right)_{\partial\hat{\Omega}_i\backslash\hat{\Gamma}}$$

$$+ \left(\hat{\phi}_s(\hat{J}\hat{\boldsymbol{\sigma}}_s \cdot \hat{\mathbf{F}}^{-T}), \hat{\nabla}\hat{\Psi}_{\mathbf{v}_s}\right)_{\hat{\Omega}_i} - \left(\hat{\phi}_s[\hat{J}(\hat{\boldsymbol{\sigma}}_s - \hat{p}\mathbf{I}) \cdot \hat{\mathbf{F}}^{-T}] \cdot \hat{\mathbf{n}}, \hat{\Psi}_{\mathbf{v}_s}\right)_{\partial\hat{\Omega}_i\backslash\hat{\Gamma}}$$

$$- \left(\hat{P}, \hat{\nabla} \cdot (\hat{J}\hat{\Psi}_{\mathbf{V}} \cdot \hat{\mathbf{F}}^{-T})\right)_{\hat{\Omega}_o} + \left(\hat{\nabla} \cdot (\hat{J}\hat{\mathbf{V}} \cdot \hat{\mathbf{F}}^{-T}), \hat{\Psi}_P\right)_{\hat{\Omega}_o}$$

$$- \left(\hat{p}, \hat{\nabla} \cdot [\hat{J}(\hat{\phi}_f\hat{\Psi}_{\mathbf{v}_f} + \hat{\phi}_s\hat{\Psi}_{\mathbf{v}_s}) \cdot \hat{\mathbf{F}}^{-T}]\right)_{\hat{\Omega}_i} + \left(\hat{\nabla} \cdot [\hat{J}(\hat{\phi}_f\hat{\mathbf{v}}_f + \hat{\phi}_s\hat{\mathbf{v}}_s) \cdot \hat{\mathbf{F}}^{-T}], \hat{\Psi}_p\right)_{\hat{\Omega}_i}$$

$$+ \left(\xi \hat{\phi}_f \hat{\phi}_s (\hat{\mathbf{v}}_f - \hat{\mathbf{v}}_s) \hat{J}, \hat{\Psi}_{\mathbf{v}_f} - \hat{\Psi}_{\mathbf{v}_s} \right)_{\hat{\Omega}_i} + \left(\frac{1}{\eta} (\hat{\mathbf{V}} - \hat{\mathbf{v}}_s) \cdot \mathbf{n}, (\hat{\Psi}_{\mathbf{V}} - \hat{\Psi}_{\mathbf{v}_s}) \cdot \mathbf{n} m \hat{J} \right)_{\hat{\Gamma}}$$

$$+ \left(\frac{1}{\beta} (\hat{\mathbf{V}} - \hat{\mathbf{v}}_s) \cdot \mathbf{T}, (\hat{\Psi}_{\mathbf{V}} - \hat{\Psi}_{\mathbf{v}_s}) m \hat{J} \right)_{\hat{\Gamma}} + \left(\frac{\hat{\phi}_f^2}{\beta} (\hat{\mathbf{v}}_f - \hat{\mathbf{v}}_s) \cdot \mathbf{T}, (\hat{\Psi}_{\mathbf{v}_f} - \hat{\Psi}_{\mathbf{v}_s}) m \hat{J} \right)_{\hat{\Gamma}} = 0, \tag{25}$$

where $m = |\hat{\mathbf{F}}^{-T} \cdot \hat{\mathbf{n}}|$, and $\hat{\mathbf{n}}$ is the unit normal in the reference frame. Here we have utilized the Piola transformation $\int_{\Omega} \nabla \cdot \mathbf{w} d\mathbf{x} = \int_{\hat{\Omega}} \hat{\nabla} \cdot (\hat{J} \hat{\mathbf{w}} \cdot \hat{\mathbf{F}}^{-T}) d\hat{\mathbf{x}}$, where $\mathbf{w}$ can be either a tensor or a vector. Special attention should be given to the surface integrals on $\hat{\Gamma}$. First, unlike field functions, the unit normal $\mathbf{n}$ in the Eulerian frame is different from $\hat{\mathbf{n}}$ and they are related by $\mathbf{n} = \frac{\hat{\mathbf{F}}^{-T} \cdot \hat{\mathbf{n}}}{m}$. Second, due to stretching of surfaces, the surface integrals are related by $\int_{\Gamma} f ds = \int_{\hat{\Gamma}} \hat{f} m \hat{J} d\hat{s}$.

In the reference frame, Eq. (4) for solid volume fraction can be cast into

$$\frac{\partial \ln \hat{\phi}_s}{\partial t} + \hat{\nabla} \hat{\mathbf{v}}_s : \hat{\mathbf{F}}^{-T} = 0 \quad \text{in } \hat{\Omega}_i. \tag{26}$$

This form has two benefits. First, if we decouple this equation from the others, then it is simply a linear ordinary differential equation for $\ln \hat{\phi}_s$. Second, $\hat{\phi}_s > 0$ is guaranteed. The weak form of Eq. (26) reads

$$\left(\frac{\partial \ln \hat{\phi}_s}{\partial t}, \hat{\Psi}_{\phi_s} \right)_{\hat{\Omega}_i} + \left(\hat{\nabla} \hat{\mathbf{v}}_s : \hat{\mathbf{F}}^{-T}, \hat{\Psi}_{\phi_s} \right)_{\hat{\Omega}_i} = 0. \tag{27}$$

The weak form for the mesh displacement and propagation (Eqs. (19), (20)) requires special attention. As we have noted before, the displacement field $\hat{\mathbf{u}}$ can be represented by a single function in the continuous finite element space. We seek solution $\hat{\mathbf{u}} \in H^1(\hat{\Omega})^d$ with corresponding test function $\hat{\Psi}_{\mathbf{u}}$. Earlier studies have used this weak form [48]:

$$\left(\frac{\partial \hat{\mathbf{u}}}{\partial t} - \hat{\mathbf{v}}_s, \hat{\Psi}_{\mathbf{u}} \right)_{\hat{\Omega}_i} + \left(\alpha \hat{\nabla} \hat{\mathbf{u}}, \hat{\nabla} \hat{\Psi}_{\mathbf{u}} \right)_{\hat{\Omega}_o} + \left(\alpha \hat{\nabla} \hat{\mathbf{u}} \cdot \hat{\mathbf{n}}, \hat{\Psi}_{\mathbf{u}} \right)_{\hat{\Gamma}} = 0. \tag{28}$$

But we have found that the relation $\frac{\partial \hat{\mathbf{u}}}{\partial t} = \hat{\mathbf{v}}_s$ is easily violated on $\hat{\Gamma}$ with significant errors, and α has to be very small to achieve reasonable accuracy. This is not surprising since the second and the third terms in Eq. (28) make the weak form inconsistent with $\frac{\partial \hat{\mathbf{u}}}{\partial t} = \hat{\mathbf{v}}_s$ on $\hat{\Gamma}$. Taking alternative forms of the surface integral on $\hat{\Gamma}$ or even removing that term completely does not resolve this issue. We thus come up with an improved formulation:

$$\left(\frac{\partial \hat{\mathbf{u}}}{\partial t} - \hat{\mathbf{v}}_s, \hat{\Psi}_{\mathbf{u}} \right)_{\hat{\Omega}_i} + c \left(\alpha \hat{\nabla} \hat{\mathbf{u}}, \hat{\nabla} \hat{\Psi}_{\mathbf{u}} \right)_{\hat{\Omega}_o} = 0 \tag{29}$$

with the slip or no-slip condition on the part of outer boundary not in contact with the hydrogel ($\partial \hat{\Omega}_o \backslash \hat{\Gamma}$), where $c = 1$ for test functions with $\hat{\Psi}_{\mathbf{u}}|_{\hat{\Gamma}} = 0$ and $c = 0$ for all other $\hat{\Psi}_{\mathbf{u}}$. It is easy to see that this equation is equivalent to

$$\left(\frac{\partial \hat{\mathbf{u}}_s}{\partial t} - \hat{\mathbf{v}}_s, \hat{\Psi}_{\mathbf{u}_s} \right)_{\hat{\Omega}_i} = 0, \quad \forall \hat{\Psi}_{\mathbf{u}_s} \in H^1(\hat{\Omega}_i)^d \tag{30}$$

and

$$\left(\alpha \hat{\nabla} \hat{\mathbf{u}}_f, \hat{\nabla} \hat{\Psi}_{\mathbf{u}_f} \right)_{\hat{\Omega}_o} = 0, \quad \forall \hat{\Psi}_{\mathbf{u}_f} \in H^1(\hat{\Omega}_o)^d \tag{31}$$

with the Dirichlet condition $\hat{\mathbf{u}}_f = \hat{\mathbf{u}}_s$ on $\hat{\Gamma}$ and the slip or no-slip condition on $\partial \hat{\Omega}_o \backslash \hat{\Gamma}$. Thus Eq. (29) enjoys the advantages of both Eq. (28) and Eqs. (30), (31): only a single function $\hat{\mathbf{u}}$ defined on the whole domain $\hat{\Omega}$ is required, there is no need to impose Dirichlet condition on the inner boundary $\hat{\Gamma}$, and $\frac{\partial \hat{\mathbf{u}}}{\partial t} = \hat{\mathbf{v}}_s$ is guaranteed on $\hat{\Gamma}$.

To sum up, in the reference frame, we seek solutions $\hat{\mathbf{V}}$, $\hat{P}$, $\hat{\mathbf{v}}_f$, $\hat{\mathbf{v}}_s$, $\hat{p}$, $\hat{\phi}_s$, and $\hat{\mathbf{u}}$ that satisfy Eqs. (25), (27), (29) for all admissible test functions, with the following constraints on the velocities and their corresponding test functions:

$$(\hat{\mathbf{V}} - \hat{\mathbf{v}}_s)\Big|_{\hat{\Gamma}} \cdot \mathbf{n} = \hat{\phi}_f (\hat{\mathbf{v}}_f - \hat{\mathbf{v}}_s)\Big|_{\hat{\Gamma}} \cdot \mathbf{n}, \tag{32}$$

$$(\hat{\Psi}_{\mathbf{V}} - \hat{\Psi}_{\mathbf{v}_s})\Big|_{\hat{\Gamma}} \cdot \mathbf{n} = \hat{\phi}_f (\hat{\Psi}_{\mathbf{v}_f} - \hat{\Psi}_{\mathbf{v}_s})\Big|_{\hat{\Gamma}} \cdot \mathbf{n}. \tag{33}$$

The unit normal $\mathbf{n}$ here is inherited from Eqs. (10), (15) and should not be confused with $\hat{\mathbf{n}}$ in the reference frame.

It should be noted that the implementation of the constraints above is non-trivial. At each node on $\hat{\Gamma}$, we identify the $\mathbf{n}$ component with the greatest magnitude. Without loss of generality, suppose n_x has the greatest magnitude. In two dimensions, Eq. (32) can then be rewritten as

$$\hat{V}_x = \frac{1}{n_x}\left(\hat{\phi}_f\hat{\mathbf{v}}_f\cdot\mathbf{n} + \hat{\phi}_s\hat{\mathbf{v}}_s\cdot\mathbf{n} - \hat{V}_y n_y\right). \tag{34}$$

Using this equation, we replace the unknown $\hat{V}_x$ by a combination of $\hat{V}_y$, $\hat{\mathbf{v}}_f$, and $\hat{\mathbf{v}}_s$ at the same node on $\hat{\Gamma}$. Similarly, $\hat{\Psi}_{\mathbf{V}_x}$ is replaced by a combination of $\hat{\Psi}_{\mathbf{V}_y}$, $\hat{\Psi}_{\mathbf{v}_f}$, and $\hat{\Psi}_{\mathbf{v}_s}$. In coding, this operation is realized by the AffineConstraints class in deal.II [49].

4.4. Numerical discretization

We solve Eqs. (25), (27), (29) with a code developed on top of the step-46 tutorial program of the open-source finite-element library deal.II [49]. The reference domain $\hat{\Omega}$ is partitioned into quadrilateral cells with $\hat{\Gamma}$ covered by cell edges. We use $Q1$ elements for $\hat{p}$ and $\hat{P}$ and $Q2$ elements for $\hat{\mathbf{V}}$, $\hat{\mathbf{v}}_f$, $\hat{\mathbf{v}}_s$, $\hat{\mathbf{u}}$, and $\hat{\phi}_s$. In the following, we only focus on the temporal discretization.

The volume fraction equation (27) is discretized by the forward Euler scheme:

$$\left(\frac{\ln\hat{\phi}_s^{n+1} - \ln\hat{\phi}_s^n}{\Delta t^n}, \hat{\Psi}_{\phi_s}\right)_{\hat{\Omega}_i} + \left(\hat{\nabla}\hat{\mathbf{v}}_s^n : (\hat{\mathbf{F}}^n)^{-T}, \hat{\Psi}_{\phi_s}\right)_{\hat{\Omega}_i} = 0, \tag{35}$$

where $\Delta t^n = t^{n+1} - t^n$ is the time step and n denotes the time level. As this equation is nonlinear in $\hat{\phi}_s^{n+1}$, we thus take a two-step approach that only involves a linear equation. We first solve

$$\left(\frac{\hat{\psi}}{\Delta t^n}, \hat{\Psi}_{\phi_s}\right)_{\hat{\Omega}_i} + \left(\hat{\nabla}\hat{\mathbf{v}}_s^n : (\hat{\mathbf{F}}^n)^{-T}, \hat{\Psi}_{\phi_s}\right)_{\hat{\Omega}_i} = 0 \tag{36}$$

to get $\hat{\psi}$, which is in the same $Q2$ finite-element space as $\hat{\phi}_s$. We then use $\hat{\phi}_s^{n+1} = \hat{\phi}_s^n\exp(\hat{\psi})$ at each node to recover $\hat{\phi}_s^{n+1}$.

The displacement equation (29) is discretized by the backward Euler scheme:

$$\left(\frac{\hat{\mathbf{u}}^{n+1} - \hat{\mathbf{u}}^n}{\Delta t^n} - \hat{\mathbf{v}}_s^{n+1}, \hat{\Psi}_{\mathbf{u}}\right)_{\hat{\Omega}_i} + c\left(\alpha\hat{\nabla}\hat{\mathbf{u}}^{n+1}, \hat{\nabla}\hat{\Psi}_{\mathbf{u}}\right)_{\hat{\Omega}_o} = 0. \tag{37}$$

Equation (25) does not involve any time derivatives and it is thus solved with the constraints of Eq. (32), (33) at time level $n+1$. Equations (25), (37) are solved together and the resulting nonlinear system is solved using Newton's method. In each Newton iteration, the linear system is solved by the direct sparse linear solver UMFPACK [50]. We stop the iteration once the L_2 norm of the residual of the nonlinear system falls below 10^{-8}. It typically takes less than five iterations to reach convergence if the solution at time level n is used as the initial guess.

The solution procedure can be summarized as follows:

(1) Create a mesh in $\hat{\Omega} = \hat{\Omega}_o \cup \hat{\Omega}_i$ with the fluid-gel interface $\hat{\Gamma} = \hat{\Omega}_o \cap \hat{\Omega}_i$ coinciding with cell edges.
(2) Set initial conditions $\hat{\mathbf{u}}^0 = 0$, $\hat{\mathbf{v}}_s^0 = 0$ (required to compute $\hat{\phi}_s^1$), and $\hat{\phi}_s^0$.
(3) For each time level $n \geq 0$, choose a proper Δt^n and perform the following steps until a steady state or a stopping time is reached.
  (i) Solve Eq. (36). Obtain $\hat{\phi}_s^{n+1}$ based on $\hat{\phi}_s^n$ and $\hat{\mathbf{v}}_s^n$.
  (ii) Solve Eqs. (25), (37) with the constraints of Eqs. (32), (33). Obtain $\hat{\mathbf{V}}^{n+1}$, $\hat{P}^{n+1}$, $\hat{\mathbf{v}}_f^{n+1}$, $\hat{\mathbf{v}}_s^{n+1}$, $\hat{p}^{n+1}$, and $\hat{\mathbf{u}}^{n+1}$ based on $\hat{\mathbf{u}}^n$ and $\hat{\phi}_s^{n+1}$.

Our code works in both 2D and 3D, and that is one of the advantages of using the deal.II platform. To avoid high computing costs, we will only use 2D numerical examples below to validate the numerical tools. Three-dimensional computations are left for future studies.

5. Numerical examples

In this section, we will use three test problems to demonstrate the robustness and accuracy of our method. Most field functions, such as $\hat{\mathbf{V}}$, $\hat{\mathbf{u}}_s$, $\hat{\mathbf{v}}_f$, $\hat{\mathbf{v}}_s$, $\hat{P}$, and $\hat{p}$, do not change their values in the coordinate transformation. Some others do, including $\hat{x}$ and $\hat{y}$. In the following, we will drop $\hat{\ }$ above the variables in the first group unless doing so causes confusion. We employ the following scaling to render the governing equations and boundary conditions dimensionless:

$$(\bar{x}, \bar{y}) = (x, y)/L_0, \quad (\bar{\mathbf{V}}, \bar{\mathbf{v}}_s, \bar{\mathbf{v}}_f) = (\mathbf{V}, \mathbf{v}_s, \mathbf{v}_f)/V_0, \quad \bar{t} = t V_0/L_0,$$
$$\bar{\mathbf{u}}_s = \mathbf{u}_s/L_0, \quad (\bar{\boldsymbol{\Sigma}}, \bar{\boldsymbol{\sigma}}_s, \bar{\boldsymbol{\sigma}}_f, \bar{P}, \bar{p}) = (\boldsymbol{\Sigma}, \boldsymbol{\sigma}_s, \boldsymbol{\sigma}_f, P, p)/\mu_s, \tag{38}$$

where the bar denotes dimensionless quantities, V_0 is the characteristic velocity, and L_0 is the characteristic length for the specific problems. The parameters can be organized into the following dimensionless groups:
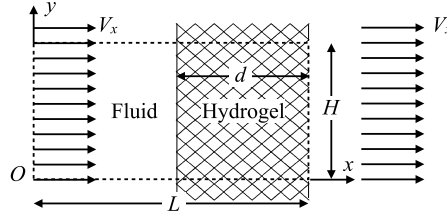
Fig. 2. Geometric setup of the 1D compression of a gel layer. We take the thickness of the gel layer to be the characteristic length L_0 such that $d = 1$. The rectangular computational domain is indicated by the dashed line, with length $L = 2$ and height $H = 1$.
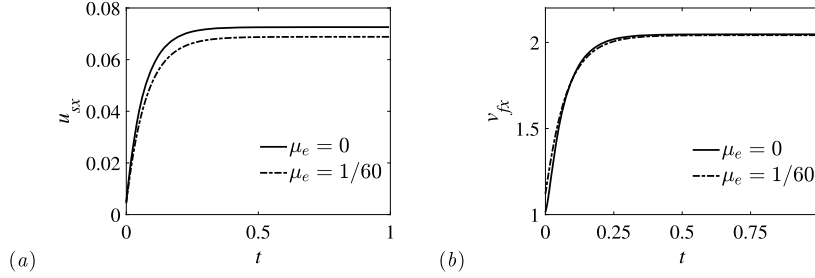

Fig. 3. The evolution of (a) the displacement $u_s|_{\hat{x}=1}$ and (b) the pore fluid velocity $v_f|_{\hat{x}=1}$ at the upstream interface $\hat{x} = 1$. The solid curves represent the Darcy flow with effective viscosity $\mu_e = 0$, and the dash-dot curves the Brinkman flow with $\mu_e = 1/60$. The other dimensionless groups governing the problem are $\lambda_s = 1$, $\xi = 2/15$, $\eta = 30$, $Ca = 1$, and $\phi_{s0} = 0.5$. The mesh size and the time step for this case are $\Delta x = 1/8$ and $\Delta t = 0.01$, respectively.

$$
\begin{aligned}
&\bar{\mu}_e = \mu_e/\mu, \quad \bar{\lambda}_s = \lambda_s/\mu_s, \quad \bar{\xi} = \xi L_0^2/\mu, \\
&(\bar{\beta}, \bar{\eta}) = (\beta, \eta)\mu/L_0, \quad Ca = V_0\mu/(L_0\mu_s), \quad \phi_{s0},
\end{aligned}
\tag{39}
$$

where ϕ_{s0} is the initial solid fraction in the undeformed hydrogel. Note that Ca indicates the ratio between the external viscous stress and the elastic stress of the solid skeleton, and can be viewed as an effective capillary number. The following discussion will only involve dimensionless variables. Therefore, we omit the bar for simplicity.

5.1. Compression of hydrogel by uniform flow

We consider a slab of hydrogel of thickness $d = 1$ that is compressed by a uniform flow of velocity $V_x = 1$ perpendicular to the gel surface (Fig. 2). The solution is one-dimensional, with no flow, deformation, or any spatial variation along the y direction. Using this as a benchmark problem for our code, however, we draw a rectangular computational domain with length $L = 2$ and height $H = 1$, and carry out the simulation in 2D. On the fluid-gel interface $\hat{x} = 1$, we impose BC1 for this benchmark problem.

The right side of the hydrogel layer is constrained so as to have zero displacement: $\mathbf{u}_s|_{\hat{x}=L} = 0$, while its left side is subject to compression by the flow. We start with a spatially uniform solid fraction $\phi_{s0} = 0.5$ at $t = 0$. The incoming flow has a constant velocity: $V_x|_{\hat{x}=0} = 1$ and $V_y|_{\hat{x}=0} = 0$. At the right surface of the gel we specify the tangential velocity $v_{fy}|_{\hat{x}=L} = 0$ and the normal traction $(-p + \sigma_{fxx})|_{\hat{x}=L} = 0$. For the top and bottom boundaries, we impose symmetry conditions such that the y-components of all the variables are put to zero, as are the $\partial/\partial y$ gradient of their x-components. For the mesh displacement $\mathbf{u}$ in the clear fluid, we impose the no-slip condition on the left boundary and the slip condition on the top and bottom boundaries. All the numerical results in this subsection are computed with a uniform Cartesian mesh of representative mesh size Δx and a fixed time step Δt.

Upon start of flow, the Darcy drag compresses the solid skeleton, and the upstream surface of the gel, at Lagrangian coordinate $\hat{x} = 1$, starts to shift in the flow direction. Fig. 3(a) shows the temporal evolution of the interfacial displacement u_{sx} toward a steady state with and without the Brinkman stress. This displacement is accompanied by an increase in the solid fraction ϕ_s and a decreases in the void fraction ϕ_f. Consequently, the fluid velocity inside the gel also rises in time to maintain fluid mass conservation, as depicted by the evolution of $v_{fx}|_{\hat{x}=1}$ at the upstream interface in Fig. 3(b). A steady state is reached when the elastic stress of the solid network balances the compression of the fluid. The Brinkman stress hinders the compression of the hydrogel, but the effect is minor for the parameters used (Fig. 3a). In the rest of this subsection, we will focus on the Darcy solution. An analytical solution is available for Darcy flow in the 1D compression (see Appendix B), and we will use it as the benchmark to validate the numerical solutions.

The steady-state solution is depicted in Fig. 4. Outside the gel, the clear fluid maintains a constant velocity $V_x = 1$ and pressure P, and so we focus on the profiles inside the gel. The Darcy drag inside the gel compresses the solid network to produce an elastic stress σ_{sxx}. As the downstream surface of the gel is fixed at $\hat{x} = 2$, the cumulative effect of compression is such that σ_{sxx} increases in magnitude along x (Fig. 4a). Consistent with this, the displacement profile u_{sx} shows the
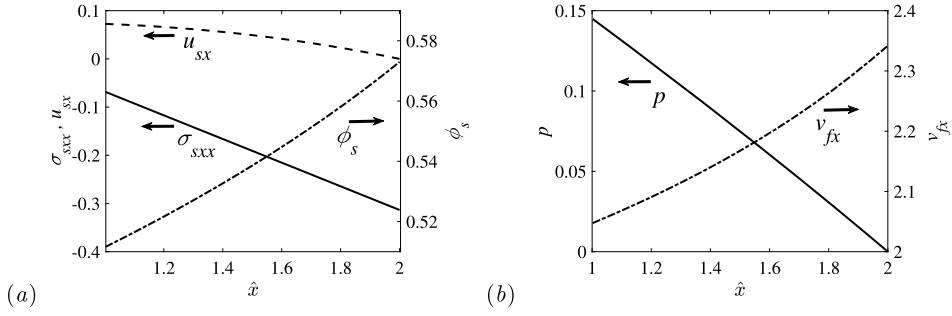
Fig. 4. Steady-state profiles for the Darcy-flow solution in the gel layer compressed by uniform flow. (a) The normal elastic stress σ_{sxx}, the displacement u_{sx}, and the solid fraction ϕ_s along the $\hat{x}$-direction. (b) The pressure p and the fluid velocity v_{fx} along the $\hat{x}$-direction. The parameters are the same as in Fig. 3 with $\mu_e = 0$.
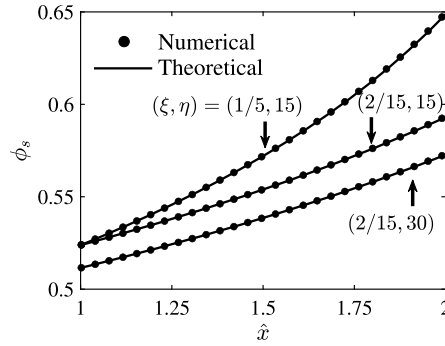

Fig. 5. Validation of the numerical solution of ϕ_s by the analytical solution of Appendix B, for three sets of moderate parameters: (ξ, η) = (1/5, 15), (2/15, 15), and (2/15, 30). The other parameters are the same as in Fig. 3 with $\mu_e = 0$. The mesh size and the time step for this case are $\Delta x = 1/8$ and $\Delta t = 0.01$, respectively.

strain $\left| \frac{\partial u_{sx}}{\partial \hat{x}} \right|$ to increase downstream, even though u_{sx} itself is greatest at the upstream surface of the gel and decreases downstream. Naturally, this increasing compression leads to a rising ϕ_s profile, the greatest compression being $\phi_s = 0.573$ at $\hat{x} = 2$ and the smallest being $\phi_s = 0.511$ at $\hat{x} = 1$.

The shrinking void fraction means that the interstitial fluid must accelerate to maintain continuity of the fluid phase, and this is indeed what the velocity profile v_{fx} shows in Fig. 4(b). Note the velocity jumps at the gel surfaces. Across the fluid-gel interface at $\hat{x} = 1$, the fluid velocity changes from $V_x = 1$ outside to $v_{fx} = 2.05$ inside the gel. At the downstream interface $\hat{x} = 2$, the fluid velocity reaches $v_{fx} = 2.34$. Note also the declining pressure in the gel layer. This negative pressure gradient acts against the Darcy drag and drives the fluid downstream (see Eq. (6)). The zero normal traction condition at $\hat{x} = 2$ reduces to $p = 0$ in the Darcy flow. Accordingly, $p = 0.145$ at the interface and the free stream takes on a constant pressure $P = 0.178$ upstream the gel layer, as dictated by the boundary condition governing normal force balance (Eq. (11)).

To benchmark our numerical solution by the analytical solution of Appendix B, we plot the profiles of the solid volume fraction $\phi_s(\hat{x})$ in Fig. 5 for three sets of parameters. The numerical solution is in excellent agreement with the analytical one, the relative error being less than 0.5% in all three cases. The other profiles, e.g. v_{fx}, p and σ_{sxx}, show similarly close agreement. As intuitively expected, the amount of compression increases with the Darcy drag coefficient ξ but decreases with the permeability η.

Finally, we explore the convergence of the numerical solution with respect to temporal and spatial resolution. Based on the time-stepping and finite-element schemes in Sec. 4.4, we expect first-order convergence with decreasing Δt and second-order convergence with refining Δx. First, we fix the mesh with $\Delta x = 1/32$, and reduce Δt gradually from 0.01 to 2.5×10^{-6}. The relative error $E_{\Delta t}$ is computed from $\phi_s|_{\hat{x}=1}$ at $t = 0.1$, before the steady-state is reached, relative to the finest $\Delta t_f = 2.5 \times 10^{-6}$: $E_{\Delta t} = |\phi_s^{\Delta t_f} - \phi_s^{\Delta t}|/\phi_s^{\Delta t_f}$. Fig. 6(a) shows approximately first-order convergence with Δt, as expected. Next, we fix $\Delta t = 5 \times 10^{-6}$, and refine the mesh by halving Δx from 1/4 down to 1/128. The relative error $E_{dx} = |\phi_s^{\Delta x} - \phi_s^{\Delta x_f}|/\phi_s^{\Delta x_f}$ is defined relative to the solution on the finest mesh $\Delta x_f = 1/128$, for $\phi_s|_{\hat{x}=1}$ at $t = 0.1$. As expected, Fig. 6(b) manifests roughly second-order convergence with refining Δx. Even at the coarsest $\Delta t = 1/4$, the relative error is only $E_{\Delta x} = 3.5 \times 10^{-5}$. It should be noted that higher spatial order may be achieved for individual variables. For example, the interfacial displacement exhibits a fourth-order convergence with refining Δx. But the overall spatial order of the whole scheme is limited by ϕ_s. For the other numerical examples presented below, we have carried out similar Δt and Δx refinements and determined the level of resolution required for accurate solutions. For brevity, we will not include results for these convergence tests in the following.
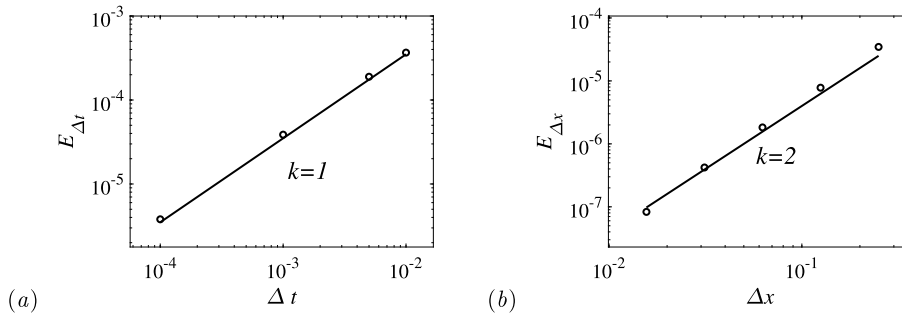
Fig. 6. (*a*) Convergence test with respect to the time step Δt. The error is for the interfacial value of solid fraction $\phi_s|_{\hat{x}=1}$ relative to the finest $\Delta t = 2.5 \times 10^{-6}$ at $t = 0.1$. The mesh size is fixed at $\Delta x = 1/32$. The solid line indicates a slope of 1. (*b*) Convergence test with respect to the mesh size Δx. The error is computed from $\phi_s|_{\hat{x}=1}$ at $t = 0.1$ relative to the finest mesh $\Delta x = 1/128$. The time step is fixed at $\Delta t = 5 \times 10^{-6}$. The solid line indicates a slope of 2. The parameters are the same as in Fig. 3 with $\mu_e = 0$.
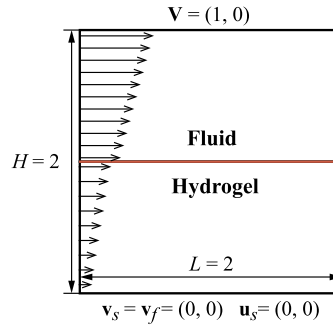
Fig. 7. The computational setup for a two-layer shear flow, with a layer of clear fluid flowing over a horizontal gel layer. The top boundary moves with a constant velocity $V_x = 1$ while the bottom is fixed. Periodic boundary conditions apply between the left and right boundaries.

5.2. Two-layer shear flow

To test the performance of our code for shear flow, we compute the two-layer shear flow of Fig. 7. A layer of clear fluid lies atop a gel layer, both of unit thickness. The top boundary moves with constant velocity of $V_x = 1$ to generate a shear flow in the fluid. The bottom boundary is fixed so the fluid velocity $\mathbf{v}_f$ and the solid displacement $\mathbf{u}_s$ are both zero. Periodic boundary conditions apply for the left and right boundaries of our domain. To remove the indeterminacy in the value of pressure, we have imposed a zero-mean constraint on p on the top boundary. To reduce mapping distortion, we impose the slip condition for $\mathbf{u}$ on the top boundary. At $t = 0$, the hydrogel has a uniform solid fraction $\phi_{s0} = 0.5$. The physical question of interest is the flow entrained in the gel layer, especially the velocity jump at the interface. Therefore, we will investigate the effects of interfacial slip coefficient β and the friction coefficient ξ.

The two-layer shear flow has been often used in the past for testing the boundary conditions between a fluid and a porous medium [31,32]. In particular, Feng and Young [42] have shown that the boundary conditions BC1 and BC2 yield qualitatively different steady-state solutions: BC1 predicts no entrained flow inside the hydrogel while BC2 does predict such a flow. Aside from using their solutions as benchmarks to validate our numerical solutions, we will also explore the solutions' dependence on the model parameters β and ξ, as well as the time transients after the top boundary starts abruptly. As it turns out, both BC1 and BC2 predict transient flows.

First, the numerical computation has confirmed that BC1 induces zero steady-state flow inside the gel, whereas BC2 entrains a steady-state shear. The latter solution is illustrated by the fluid velocity and solid displacement profiles in Fig. 8. The most notable feature is perhaps the discontinuity in tangential velocity across the interface. This arises from BC2 that assumes such a "slip" to be proportional to the shear stress in the clear fluid (Eq. (13)). In contrast, BC1 stipulates that the fluid velocity in the gel be proportional to the Brinkman shear stress inside the gel (Eq. (12)). With the fixed boundary at the bottom, this leads to zero flow in the steady state. With BC2, the fluid flow exerts a Darcy drag on the solid phase, producing the displacement profile u_{sx}. Since $\mathcal{F}_x^{f \to s} > 0$, the solid-phase force balance (Eq. (7)) implies a negative y-gradient in the solid shear stress. This is why the displacement profile $u_{sx}(\hat{y})$ exhibits an upward concavity. Similarly, $v_{fx}(\hat{y})$ exhibits a downward concavity because $\mathcal{F}_x^{s \to f} = -\mathcal{F}_x^{f \to s} < 0$. Also shown in Fig. 8 are profiles from the analytical solution of Feng and Young [42]. The numerical solution agrees with the analytical one within 1%, providing additional validation for the numerical algorithm.

There is a subtlety in the above comparison with the analytical solution. The latter can be easily obtained only for a linearly elastic solid [42]. Therefore, the agreement is meaningful only in the limit of small displacement, which is largely
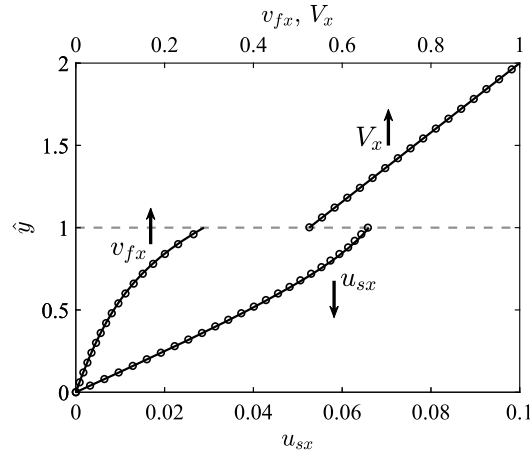
Fig. 8. The steady-state profiles in the two-layer shear flow, with boundary conditions BC2 on the fluid-gel interface and dimensionless parameters $\mu_e = 1$, $\lambda_s = 1$, $\xi = 10$, $\beta = 0.5$, $\eta = 1$, $Ca = 0.1$, and $\phi_{s0} = 0.5$. The clear fluid has a linear profile $V_x(\hat{y})$ as expected, while inside the gel, nonlinear $v_{fx}(\hat{y})$ and $u_{sx}(\hat{y})$ profiles are entrained. The symbols denote the numerical results while the solid lines are theoretical solutions for a linearly elastic solid phase in the gel [42].
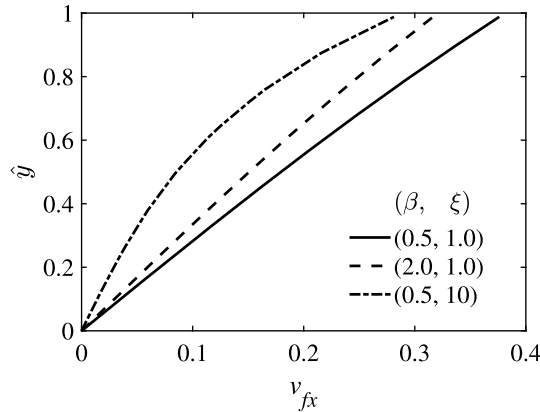
Fig. 9. Effects of the interfacial slip coefficient β and Darcy drag coefficient ξ on the shear velocity profile inside the gel layer. We have adopted BC2 on the fluid-gel interface. $(\beta, \xi) = (0.5, 1.0)$, $(2.0, 1.0)$, and $(0.5, 10)$ from bottom to top. The other dimensionless parameters are the same as in Fig. 8.

satisfied in the u_{sx} range of Fig. 8. But note that the numerical solution falls increasingly short of the analytical u_{sx} toward the interface, as the magnitude of u_{sx} surpasses 0.06. This is not a numerical error but a manifestation of the nonlinear elasticity in the solid skeleton. In addition, the Saint Venant-Kirchhoff equation predicts a small positive normal stress σ_{syy} when a simple shear is imposed, implying a slight vertical shrinkage of the gel layer. For the parameters of Fig. 8, the interface shifts slightly downward, by about 0.002, relative to the undeformed state.

In a parametric study, we explore how the steady-state shear flow inside the gel depends on the interfacial slip coefficient β and the Darcy drag coefficient ξ (Fig. 9). With a relatively small Darcy drag ($\xi = 1$), the velocity profile $v_{fx}(\hat{y})$ is almost linear, as the flow is mostly driven by the velocity on the interface $v_i = v_{fx}|_{\hat{y}=1}$ as if in a simple shear flow. The interfacial velocity v_i decreases with the slip coefficient β, according to the tangential slip velocity condition of BC2 (Eq. (13)). Increasing ξ from 1 to 10 not only hinders the fluid flow everywhere inside the gel, but also increases the downward concavity of the v_{fx} profile. We are testing very large pores to highlight the velocity profiles. For realistic pore sizes (e.g. $\xi = 1000$), the velocity inside the gel will be much reduced.

To end this subsection, let us examine the temporal development of the flow inside the gel layer after inception of the shear flow. Initially all fluid and solid components are at rest. At $t = 0$, the top boundary abruptly starts to move with $V_x = 1$. Note first that the momentum equations for both phases are inertialess (Eqs. (6), (7)). Thus, time-dependence comes solely from the transient deformation of the skeletal phase (Eq. (8)). As the solid skeleton starts from a state of zero strain and zero stress, it offers no initial resistance to the Darcy drag. Thus, initially $\mathbf{v}_f = \mathbf{v}_s$ throughout the gel, with both components moving with the same velocity. For the lack of Darcy drag, the fluid flow $\mathbf{v}_f$ is fastest at the start, and it decays in time as the Darcy drag develops. The initial velocity discontinuity across the fluid-gel interface is governed by the shear stress of the clear fluid: $V_x - v_{fx} = V_x - v_{sx} = \beta \Sigma_{xy}$. The above observations about the initial moment apply to both BC1 and BC2.
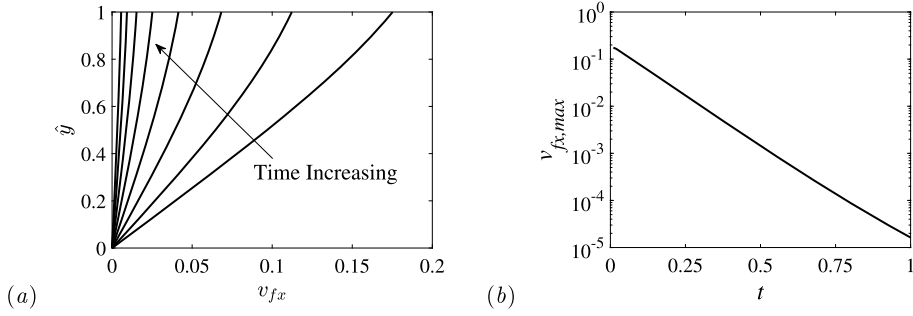
Fig. 10. The temporal evolution of the velocity field inside the layer of hydrogel with BC1. The dimensionless parameters are the same as in Fig. 8. (*a*) The evolution of the velocity profile $v_{fx}(\hat{y})$ from $t = 0.05$ to 0.4 with a constant time interval of 0.05. (*b*) The evolution of the fluid velocity at the interface, also the maximum velocity in the hydrogel. The velocity field approaches zero eventually, which is consistent with the theoretical prediction.
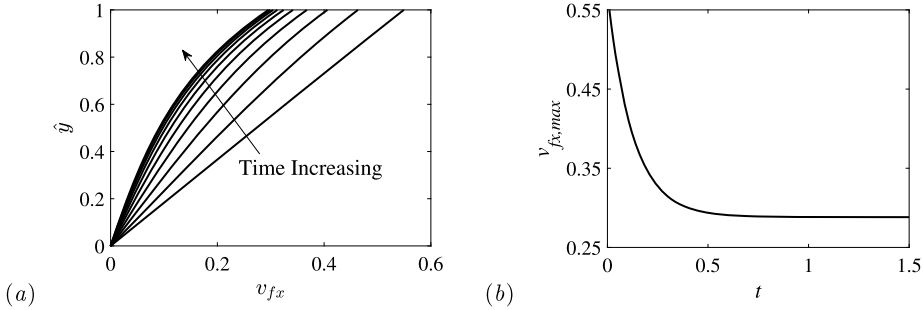

Fig. 11. The temporal evolution of the velocity field inside the layer of hydrogel with BC2 with parameters $(\beta, \xi) = (0.5, 10)$. (*a*) The variation of velocity along y-direction(vertical) of the ten different time t from 0.05 to 0.5. (*b*) The evolution of the fluid velocity at the interface, also the maximum velocity in the hydrogel.

But the subsequent development differs. More quantitatively, BC1 relates the slip velocity between the two phases to the Brinkman shear stress σ_{fxy} on the gel side of the interface (Eq. (12)):

$$\phi_f(v_{fx} - v_{sx}) = -\beta\sigma_{fxy}. \tag{40}$$

As the early velocity profile of Fig. 10(*a*) shows, $\sigma_{fxy} > 0$. Consequently, the fluid velocity always lags the solid velocity. As the solid elastic stress builds up, the solid deformation slows down, with $v_{sx} \to 0$. Thus, the fluid inside the gel comes to rest in time as well (Fig. 10*b*). In contrast, BC2 determines the slip velocity between the two phases by the solid shear stress σ_{sxy} (Eq. (13)):

$$\phi_s(v_{sx} - v_{fx}) = -\beta\sigma_{sxy}. \tag{41}$$

As the solid network deforms, σ_{sxy} builds up in time while $v_{sx} \to 0$. On balance, v_{fx} sees a relatively mild decay in time (Fig. 11b).

5.3. Deformation of a Darcy particle in planar elongational flow

A planar elongational flow has hyperbolic streamlines that collide along the horizontal *x*-axis and separate along the vertical *y*-axis (Fig. 12a). When a circular particle of Darcy hydrogel, with the effective viscosity μ_e set to zero and the Brinkman stress omitted, is placed at the center of the flow, it will be squeezed horizontally and stretched vertically. We will use our code to compute the flow and deformation in this problem. Note that omitting the Brinkman stress term in the momentum equation of the fluid (Eq. (6)) removes $\nabla^2 \mathbf{v}_f$. Thus, we will no longer need the third boundary condition for the tangential slip velocity in BC1 (Eq. (12)).

For symmetry, we take the computational domain to be a circular sector covering the first quadrant of the flow (Fig. 12a). We choose the characteristic length L_0 to be the initial particle radius and the characteristic velocity $V_0 = \varepsilon L_0$, where ε is the undisturbed elongation rate. In dimensionless terms, the undeformed particle has a radius of $R = 1$ and the domain has a radius of 35 to ensure negligible boundary effects. Symmetry conditions are imposed on the *x* and *y* axes, while on the external boundary we impose the velocity of the undisturbed flow field: $(V_x, V_y)|_{r=35} = (-x, y)$, where $r = \sqrt{x^2 + y^2}$. The mean value of P is set to zero on the external boundary to remove indeterminacy in the value of pressure. For the mesh displacement $\mathbf{u}$ in the clear fluid, we impose the no-slip condition on the external boundary and the slip condition on the *x* and *y* axes. To ensure proper spatial resolution, we employ a spatially graded meshing scheme with three levels of mesh
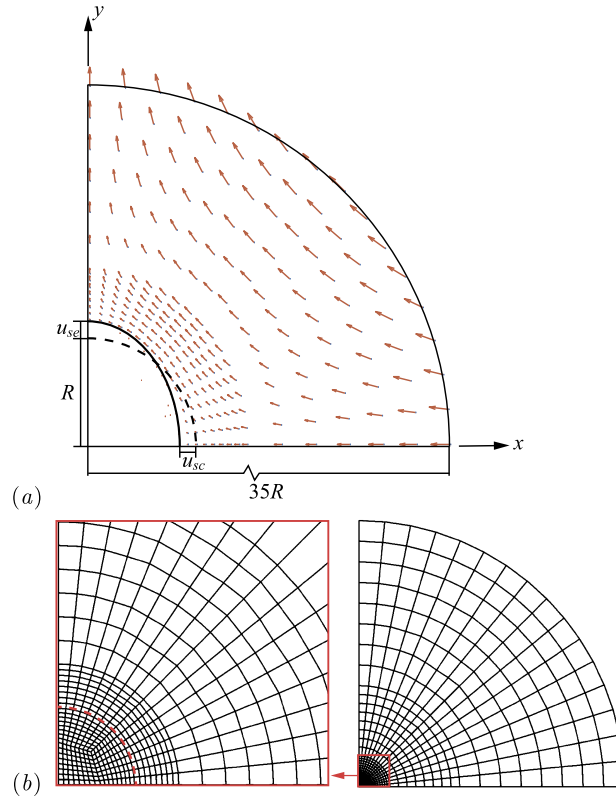
Fig. 12. (*a*) Planar elongation of the exterior fluids deforms a Darcy gel particle centered at the origin. The undeformed particle has a radius $R = 1$, and the steady-state deformation of the particle is measured by the elongation at the north pole (u_{se}) and the compression at the equator (u_{sc}). (*b*) The mesh with minimum mesh size $h_{min} = 0.06$ inside the particle and maximum $h_{max} = 3$ along the exterior boundary, with a magnified view of the dense mesh around the particle. The red dash line is the initial location of the interface of the Darcy particle. (For interpretation of the colors in the figure(s), the reader is referred to the web version of this article.)
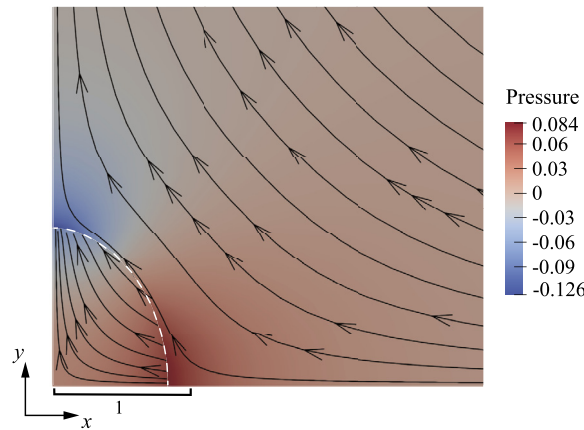

Fig. 13. Steady state streamlines and pressure contours around the Darcy gel particle, with dimensionless parameters $Ca = 0.0375$, $\xi = 400$, $\eta = 0.0025$, $\beta = 0.5$, $\lambda_s = 1$, and $\phi_{s0} = 0.5$. The white dash line delineates the steady-state interface between the gel particle and the pure fluid.

sizes, with the finest inside the particle and the coarsest in the far field of the flow (Fig. 12*b*). Refinements in the mesh size and time step have shown that those used are adequate for accurate solution. The error in ϕ_s is consistent with the second-order mesh convergence.

The steady-state solution is depicted by the streamlines and pressure contours in Fig. 13 and the velocity and pressure profiles along the x and y axes in Fig. 14. For this solution, the effective capillary number $Ca = \varepsilon \mu / \mu_s = 0.0375$ is high enough to produce considerable deformation in the gel particle. The porosity of the gel and the permeation and slip coefficients are such that its surface presents considerable resistance to fluid penetration. Thus, on approaching the gel along the
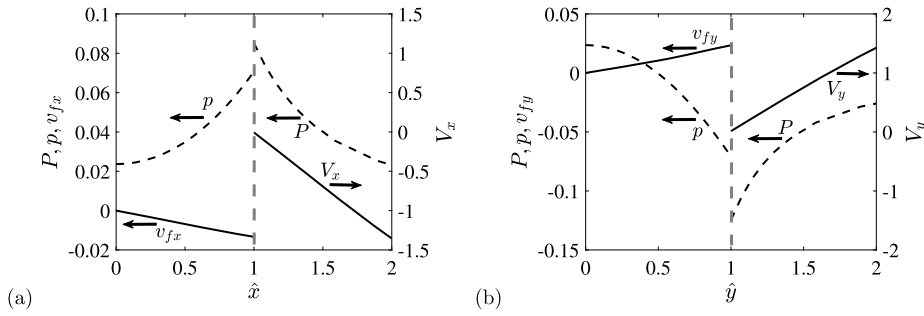
Fig. 14. (a) The pressure and fluid velocity profiles inside ($\hat{x} < 1$) and outside the gel ($\hat{x} > 1$) along the x-axis. Note the different velocity scales inside and outside the gel. (b) Similar profiles along the y-axis. In both plots, the gray dash line marks the location of interface.
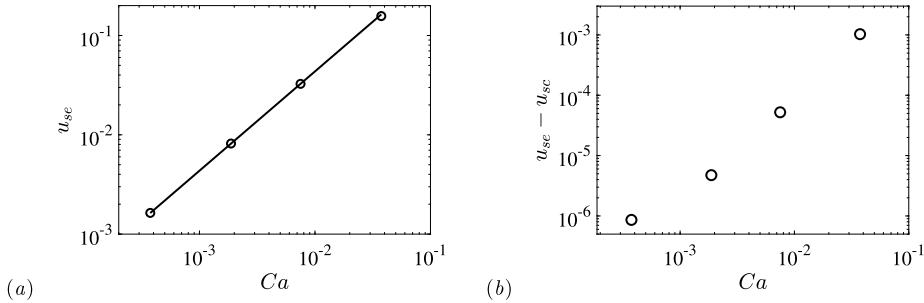

Fig. 15. (a) Gel particle deformation at the north pole u_{se} increases with the effective capillary number Ca. The other dimensionless parameters are fixed at the values of Fig. 13. The numerical results (symbols) are also compared with analytical solutions for the limit of small deformation (lines). (b) The difference of the two measures of deformation, u_{se} and u_{sc}.

x-axis, the magnitude of the incoming velocity $|V_x|$ drops to 6.270×10^{-3} at the upstream "stagnation point" $(\hat{x}, \hat{y}) = (1, 0)$ (Fig. 14a). Just inside the gel, $|v_{fx}| = 1.333 \times 10^{-2}$, maintaining fluid mass conservation (Eq. (10)) according to the local porosity $\phi_f = 0.471$. Thus, the streamlines appear to be discontinuous at the interface (Fig. 13). Most of the external streamlines go around the gel particle, and only those close to the x-axis end up penetrating the interface to produce the Darcy flow inside. Meanwhile, the pressure P rises toward the interface as if in a flow around an impermeable particle. Inside the gel, Darcy drag causes the pressure p to drop along the internal streamlines. The profiles of Fig. 14(b) at the downstream "stagnation point" $(\hat{x}, \hat{y}) = (0, 1)$ can be interpreted in similar ways.

Fig. 15(a) plots the interfacial displacement u_{se} at the north pole (i.e., the gel-particle elongation) as a function of the effective capillary number Ca. The numerical data exhibit a simple proportionality $u_{se} \propto Ca$. Besides, we also compare the numerical solution to an analytical solution valid in the small-deformation limit. Young et al. [41] calculated the deformation of a Darcy particle in a uniaxial elongational flow in the limit of small deformation. It turns out that a similar solution can be derived in the planar elongational flow as well (Appendix C), and it serves as a benchmark for our numerical solution in Fig. 15(a). The difference is a mere 0.2% for the small deformation at $Ca = 3.75 \times 10^{-4}$. With increasing Ca, the numerical solution increasingly falls below the analytical formula, reaching a difference of 3.8% at $Ca = 0.0375$.

The analytical solution shows that in the limit of small deformation, the two measures of the deformation of hydrogel, u_{se} and u_{sc}, are exactly the same. Our numerical results show greater compression at the equator than the elongation at the pole: $u_{sc} > u_{se}$, and the difference $\Delta u = u_{sc} - u_{se}$ increases with Ca (Fig. 15b). For small Ca, Δu approaches zero as expected from the theoretical solution.

If we continue to increase the elongation rate, at a certain threshold the code fails to produce a steady-state solution. This is illustrated by the snapshots in Fig. 16 for $Ca = 0.075$, which also depict the instantaneous ϕ_s distribution inside the gel particle. As the particle stretches gradually in the vertical direction, two sharp points eventually form at the two poles of the particle, where the solid fraction also decreases markedly. Finally, our simulation diverges due to the emerging singularity at the poles. This may correspond to a physical situation of a loss of steady-state solution. Such a behavior can be likened to the well-known tip-streaming on highly stretched liquid drops [51,52].

6. Concluding remarks

This paper presents a finite-element method to compute two-phase flows that involve a clear solvent fluid outside a hydrogel, with potential solvent permeation into the gel. From a theoretical viewpoint, this problem is complicated by open questions about the boundary conditions that should be posed on the interface. As long as one adopts a coarse-grained mixture model for the gel, pore-scale morphological information is lost. This implies an insufficient number of boundary
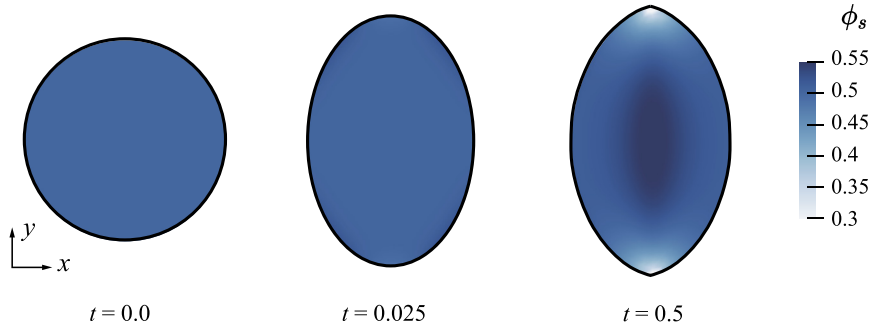
Fig. 16. Cusp formation on a highly deformed gel particle at $Ca = 0.075$, with severely reduced solid fraction at the tips. The computation fails to converge to a steady-state solution in this case.

conditions, based on the overall mass and force balance alone, for solving for the motion of both the fluid and solid phases inside the gel. We have adopted additional boundary conditions from recent work that ensures positive entropy production at the fluid-gel interface. Thus, we have a mathematically well-posed problem.

To compute nontrivial fluid-gel two-phase flows, one has to deal with two numerical challenges. The first is to implement the unconventional and complex boundary conditions in a finite-element framework. This has been resolved by imposing constraints on the test functions for different unknown variables that are constrained by the boundary conditions. Second, we must resolve the interfacial motion accurately and efficiently in essentially a fluid-structure interaction problem. This is handled by adopting a fixed-grid arbitrary Lagrangian-Eulerian method that maps the deformed domain and mesh back onto a fixed reference domain and mesh at each time step.

To validate the computational tool, we have applied it to three test problems: one-dimensional compression of a hydrogel layer by a uniform flow normal to the layer, two-layer shear flow with a clear fluid flowing above a gel layer, and finally, the deformation of a Darcy particle at the stagnation point of a planar elongational flow. In all three cases, we have derived analytical solutions, at least under limiting conditions, to benchmark the numerical solutions. The comparisons have confirmed the accuracy of the latter, and further established the order of convergence with respect to refinements in mesh size and time step. Thus, we have developed a numerical package based on the finite-element library deal.II.

The algorithm and codes developed herein can be applied to explore a wide range of problems. These include fundamental two-phase flow problems involving a hydrogel, biological modeling of the cytoplasm during cell migration, as well as engineering design and optimization in deploying hydrogels in microfluidic devices for culturing cells and tissues.

CRediT authorship contribution statement

Lei Li: Methodology, Software, Writing – original draft. **Jiaqi Zhang:** Methodology, Software, Validation, Writing – review & editing. **Zelai Xu:** Data curation, Validation, Writing – original draft. **Y.-N. Young:** Methodology, Writing – review & editing. **James J. Feng:** Conceptualization, Methodology, Supervision, Writing – review & editing. **Pengtao Yue:** Conceptualization, Methodology, Software, Supervision, Writing – review & editing.

Declaration of competing interest

The authors declare that they have no known competing financial interests or personal relationships that could have appeared to influence the work reported in this paper.

Acknowledgements

Appendix A. Inner products on Γ in the weak form

In this appendix, we explain how to obtain the surface integrals on Γ in the weak form of Eq. (14). To shorten the derivation, we only consider the combined weak form of Eqs. (2), (6), (7). By taking the inner products of Eq. (2) with $\Psi_{\mathbf{V}}$ in Ω_o, Eq. (6) with $\Psi_{\mathbf{V}_f}$ in Ω_i, and Eq. (7) with $\Psi_{\mathbf{V}_s}$, performing integration by parts, and summing them up, we get

$$
(\mathbf{\Sigma}, \nabla \Psi_{\mathbf{V}})_{\Omega_o} - ((\mathbf{\Sigma} - P\mathbf{I}) \cdot \mathbf{n}, \Psi_{\mathbf{V}})_{\partial \Omega_o \setminus \Gamma} + ((\mathbf{\Sigma} - P\mathbf{I}) \cdot \mathbf{n}, \Psi_{\mathbf{V}})_{\Gamma}
$$

$$
+ \left(\phi_f \boldsymbol{\sigma}_f, \nabla \Psi_{\mathbf{v}_f}\right)_{\Omega_i} - \left(\phi_f (\boldsymbol{\sigma}_f - p\mathbf{I}) \cdot \mathbf{n}, \Psi_{\mathbf{v}_f}\right)_{\partial \Omega_i \setminus \Gamma} - \left(\phi_f (\boldsymbol{\sigma}_f - p\mathbf{I}) \cdot \mathbf{n}, \Psi_{\mathbf{v}_f}\right)_{\Gamma}
$$

$$
+ \left(\phi_s \boldsymbol{\sigma}_s, \nabla \Psi_{\mathbf{v}_s}\right)_{\Omega_i} - \left(\phi_s (\boldsymbol{\sigma}_s - p\mathbf{I}) \cdot \mathbf{n}, \Psi_{\mathbf{v}_s}\right)_{\partial \Omega_i \setminus \Gamma} - \left(\phi_s (\boldsymbol{\sigma}_s - p\mathbf{I}) \cdot \mathbf{n}, \Psi_{\mathbf{v}_s}\right)_{\Gamma}
$$

$$
= 0, \tag{A.1}
$$

where we have partitioned $\partial \Omega_i$ and $\partial \Omega_o$ into Γ and another portion on the outer boundary. The unit normal $\mathbf{n}$ points from Ω_i to Ω_o on Γ and outwards elsewhere. We are only interested in the inner products on Γ:

$$
S = ((\mathbf{\Sigma} - P\mathbf{I}) \cdot \mathbf{n}, \Psi_{\mathbf{V}})_{\Gamma} - \left(\phi_f (\boldsymbol{\sigma}_f - p\mathbf{I}) \cdot \mathbf{n}, \Psi_{\mathbf{v}_f}\right)_{\Gamma} - \left(\phi_s (\boldsymbol{\sigma}_s - p\mathbf{I}) \cdot \mathbf{n}, \Psi_{\mathbf{v}_s}\right)_{\Gamma}. \tag{A.2}
$$

To proceed, we decompose velocity vectors and their test functions into tangential (denoted by subscript $_\parallel$) and normal (denoted by subscript $_\perp$) components. Taking $\mathbf{V}$ as example, we have $\mathbf{V} = \mathbf{V}_\parallel + \mathbf{V}_\perp$, where $\mathbf{V}_\perp = \mathbf{V} \cdot (\mathbf{n} \otimes \mathbf{n})$ and $\mathbf{V}_\parallel = \mathbf{V} - \mathbf{V}_\perp = \mathbf{V} \cdot (\mathbf{I} - \mathbf{n} \otimes \mathbf{n})$. For convenience, we introduce the projection tensor $\mathbf{T} = (\mathbf{I} - \mathbf{n} \otimes \mathbf{n})$ such that $\mathbf{V}_\parallel = \mathbf{V} \cdot \mathbf{T}$.

The mass balance condition of Eq. (10) can be rewritten as

$$
\mathbf{V}_\perp - \mathbf{v}_{s\perp} = \phi_f (\mathbf{v}_{f\perp} - \mathbf{v}_{s\perp}) \text{ on } \Gamma. \tag{A.3}
$$

We freeze ϕ_f such that this relation is linear. This can be achieved if we decouple the volume fraction equation from the equations for $\mathbf{V}$, $\mathbf{v}_f$, and $\mathbf{v}_s$. Consequently, the velocity variations, i.e., their test functions, satisfy

$$
\Psi_{\mathbf{V}\perp} - \Psi_{\mathbf{v}_s\perp} = \phi_f (\Psi_{\mathbf{v}_f\perp} - \Psi_{\mathbf{v}_s\perp}) \text{ on } \Gamma. \tag{A.4}
$$

Then we can rewrite S as

$$
\begin{aligned}
S &= \left((\mathbf{\Sigma} - P\mathbf{I}) \cdot \mathbf{n}, (\Psi_{\mathbf{V}\perp} - \Psi_{\mathbf{v}_s\perp}) + (\Psi_{\mathbf{V}\parallel} - \Psi_{\mathbf{v}_s\parallel}) + \Psi_{\mathbf{v}_s}\right)_{\Gamma} \\
&\quad - \left(\phi_f (\boldsymbol{\sigma}_f - p\mathbf{I}) \cdot \mathbf{n}, (\Psi_{\mathbf{v}_f\perp} - \Psi_{\mathbf{v}_s\perp}) + (\Psi_{\mathbf{v}_f\parallel} - \Psi_{\mathbf{v}_s\parallel}) + \Psi_{\mathbf{v}_s}\right)_{\Gamma} \\
&\quad - \left(\phi_s (\boldsymbol{\sigma}_s - p\mathbf{I}) \cdot \mathbf{n}, \Psi_{\mathbf{v}_s}\right)_{\Gamma} \\
&= \left([(\mathbf{\Sigma} - P\mathbf{I}) - (\boldsymbol{\sigma}_f - p\mathbf{I})] \cdot \mathbf{n}, \Psi_{\mathbf{V}\perp} - \Psi_{\mathbf{v}_s\perp}\right)_{\Gamma} \\
&\quad + \left((\mathbf{\Sigma} - P\mathbf{I}) \cdot \mathbf{n}, \Psi_{\mathbf{V}\parallel} - \Psi_{\mathbf{v}_s\parallel}\right)_{\Gamma} - \left(\phi_f (\boldsymbol{\sigma}_f - p\mathbf{I}) \cdot \mathbf{n}, \Psi_{\mathbf{v}_f\parallel} - \Psi_{\mathbf{v}_s\parallel}\right)_{\Gamma} \\
&\quad + \left([(\mathbf{\Sigma} - P\mathbf{I}) - (\phi_f \boldsymbol{\sigma}_f + \phi_s \boldsymbol{\sigma}_s - p\mathbf{I})] \cdot \mathbf{n}, \Psi_{\mathbf{v}_s}\right)_{\Gamma} \\
&= \left(\mathbf{n} \cdot [(\mathbf{\Sigma} - P\mathbf{I}) - (\boldsymbol{\sigma}_f - p\mathbf{I})] \cdot \mathbf{n}, (\Psi_{\mathbf{V}} - \Psi_{\mathbf{v}_s}) \cdot \mathbf{n}\right)_{\Gamma} \\
&\quad + \left([(\mathbf{\Sigma} - P\mathbf{I}) \cdot \mathbf{n}] \cdot \mathbf{T}, \Psi_{\mathbf{V}} - \Psi_{\mathbf{v}_s}\right)_{\Gamma} - \left([\phi_f (\boldsymbol{\sigma}_f - p\mathbf{I}) \cdot \mathbf{n}] \cdot \mathbf{T}, \Psi_{\mathbf{v}_f} - \Psi_{\mathbf{v}_s}\right)_{\Gamma} \\
&= \left(\mathbf{n} \cdot [(\mathbf{\Sigma} - P\mathbf{I}) - (\boldsymbol{\sigma}_f - p\mathbf{I})] \cdot \mathbf{n}, (\Psi_{\mathbf{V}} - \Psi_{\mathbf{v}_s}) \cdot \mathbf{n}\right)_{\Gamma} \\
&\quad + \left((\mathbf{\Sigma} \cdot \mathbf{n}) \cdot \mathbf{T}, \Psi_{\mathbf{V}} - \Psi_{\mathbf{v}_s}\right)_{\Gamma} - \left(\phi_f (\boldsymbol{\sigma}_f \cdot \mathbf{n}) \cdot \mathbf{T}, \Psi_{\mathbf{v}_f} - \Psi_{\mathbf{v}_s}\right)_{\Gamma},
\end{aligned} \tag{A.5}
$$

where we have used Eq. (A.4) in the second equality, traction balance of Eq. (11) in the third equality, and $(\mathbf{I} \cdot \mathbf{n}) \cdot \mathbf{T} = 0$ in the last equality.

By plugging in BC1 of Eq. (12), we can obtain the inner products on Γ that appear in Eq. (14):

$$
\begin{aligned}
S &= \left(\frac{1}{\eta} (\mathbf{V} - \mathbf{v}_s) \cdot \mathbf{n}, (\Psi_{\mathbf{V}} - \Psi_{\mathbf{v}_s}) \cdot \mathbf{n}\right)_{\Gamma} + \left(\frac{1}{\beta} (\mathbf{V} - \mathbf{v}_s) \cdot \mathbf{T}, \Psi_{\mathbf{V}} - \Psi_{\mathbf{v}_s}\right)_{\Gamma} \\
&\quad + \left(\frac{\phi_f^2}{\beta} (\mathbf{v}_f - \mathbf{v}_s) \cdot \mathbf{T}, \Psi_{\mathbf{v}_f} - \Psi_{\mathbf{v}_s}\right)_{\Gamma}.
\end{aligned} \tag{A.6}
$$

The term S for BC2 of Eq. (13) can be derived in a similar way:

$$
\begin{aligned}
S &= \left(\frac{1}{\eta} (\mathbf{V} - \mathbf{v}_f) \cdot \mathbf{n}, (\Psi_{\mathbf{V}} - \Psi_{\mathbf{v}_f}) \cdot \mathbf{n}\right)_{\Gamma} + \left(\frac{1}{\beta} (\mathbf{V} - \mathbf{v}_f) \cdot \mathbf{T}, \Psi_{\mathbf{V}} - \Psi_{\mathbf{v}_f}\right)_{\Gamma} \\
&\quad + \left(\frac{\phi_f^2}{\beta} (\mathbf{v}_f - \mathbf{v}_s) \cdot \mathbf{T}, \Psi_{\mathbf{v}_f} - \Psi_{\mathbf{v}_s}\right)_{\Gamma}.
\end{aligned} \tag{A.7}
$$

Appendix B. Theoretical solution of 1D compression

For the steady-state 1D compression by a uniform flow discussed in Sec. 5.1, an analytical solution can be obtained in the limit of Darcy flow, i.e. when the Brinkman stress term is dropped in favor of the Darcy drag and pressure gradient. The algebra is simplest if we use $\phi_s(x)$ as the primary unknown function.

With Darcy flow in the gel, the momentum equations for the fluid and solid phases can be written as

$$-\phi_f \frac{dp}{dx} - \xi \phi_s \phi_f v_f = 0, \tag{B.1}$$

$$\frac{d(\phi_s \sigma_s)}{dx} - \phi_s \frac{dp}{dx} + \xi \phi_s \phi_f v_f = 0, \tag{B.2}$$

where σ_s is a shorthand for the solid normal stress σ_{sxx}. Eliminating the pressure gradient between the two equations gives us

$$\frac{d(\phi_s \sigma_s)}{dx} = -\xi \phi_s v_f. \tag{B.3}$$

The solid normal stress σ_s obeys the St. Venant-Kirchhoff constitutive equation:

$$\sigma_s = \frac{M}{2}(-2c + c^2)(1 - c), \tag{B.4}$$

where $M = (2\mu_s + \lambda_s)$, and $c = -du_s/d\hat{x}$ is the negative displacement gradient. The fluid velocity v_f can be related to the incoming velocity of the pure fluid V_x outside the gel through the fluid continuity Eq. (3) and the boundary condition of Eq. (10): $v_f = V_x/(1 - \phi_s)$. Now the momentum balance of Eq. (B.3) becomes:

$$\frac{d\left[\phi_s \frac{M}{2}(-2c + c^2)(1 - c)\right]}{dx} = -\frac{\xi \phi_s V_x}{1 - \phi_s}. \tag{B.5}$$

To turn this into an equation for $\phi_s(x)$ only, we relate c and ϕ_s through the conservation of solid volume:

$$\phi_{s0} = \phi_s \hat{J}, \tag{B.6}$$

where ϕ_{s0} is the initial volume fraction of the solid and $\hat{J}$ is the determinant of deformation gradient. For 1D compression, the determinant can be written as

$$\hat{J} = 1 + \frac{du_s}{d\hat{x}} = 1 - c, \tag{B.7}$$

which gives

$$c = 1 - \frac{\phi_{s0}}{\phi_s}. \tag{B.8}$$

Substituting this into Eq. (B.5), we have

$$\frac{d\phi_s}{dx} = \frac{\xi \phi_s^4 V_x}{M \phi_{s0}^3 (1 - \phi_s)}. \tag{B.9}$$

To validate the steady-state numerical solution on the deformed gel, it is more convenient to use the Lagrangian coordinate $\hat{x}$ than the Eulerian x:

$$\frac{d\phi_s}{dx} = \frac{d\phi_s}{d\hat{x}} \frac{1}{1 - c} = \frac{d\phi_s}{d\hat{x}} \frac{\phi_s}{\phi_{s0}}. \tag{B.10}$$

Now Eq. (B.9) can be rewritten as

$$\frac{d\phi_s}{d\hat{x}} = K \frac{\phi_s^3}{1 - \phi_s}, \tag{B.11}$$

where $K = \frac{\xi V_x}{M \phi_{s0}^2}$.

At the upstream boundary of the gel $\hat{x} = 1$, the value of $\phi_s(\hat{x} = 1) = \phi_{s1}$ can be determined from BC1 and the solid constitutive equation. With the Brinkman stress omitted, the traction balance of Eq. (11) reduces to $\phi_s \sigma_s = p - P$. Meanwhile, the permeation condition of Eq. (12) reduces to $-V_x = \eta(p - P)$. Thus, $\eta \phi_s \sigma_s = -V_x$ is a constant on the gel interface $\hat{x} = 1$. Together with Eqs. (B.4) and (B.8), this yields

$$\phi_{s1} = \phi_s|_{\hat{x}=1} = \phi_{s0}\sqrt{\frac{M\eta\phi_{s0}}{M\eta\phi_{s0} - 2V_x}}. \tag{B.12}$$

Integrating Eq. (B.11) with this above initial condition, we obtained the analytical equation:

$$\phi_s = \frac{1 - \sqrt{1 - \kappa(x)}}{\kappa(x)} \tag{B.13}$$

where $\kappa(x) = (2\phi_{s1} - 1)/\phi_{s1}^2 + 2Kx$. Note that we have used the original dimensional symbols in this Appendix, and the formulas can be easily rendered dimensionless for comparisons in Sec. 5.1.

Appendix C. Small deformation of a Darcy particle in a planar elongational flow

For the Darcy particle in planar elongational flow discussed in Sec. 5.3, the steady-state solution can be obtained analytically in the limit of small deformation. In the following we adopt dimensional notations, and the final solution can be converted to dimensionless form for comparison with the numerical solution (Fig. 15).

C.1. Flow inside the Darcy particle

At steady state, the velocity of the solid phase of the gel vanishes, $\mathbf{v}_s = 0$. Thus the continuity and momentum equations (Eqs. (5), (6), (7)) can be simplified as

$$\nabla \cdot (\phi_f \mathbf{v}_f) = 0, \tag{C.1}$$

$$-\nabla p - \xi\phi_s\mathbf{v}_f = 0, \tag{C.2}$$

$$\nabla \cdot (\phi_s \boldsymbol{\sigma}_s) - \phi_s\nabla p + \xi\phi_f\phi_s\mathbf{v}_f = 0. \tag{C.3}$$

Furthermore, the hyperelasticity of the solid phase reduces to linear elasticity in the limit of small deformation:

$$\boldsymbol{\sigma}_s = 2\mu_s\mathbf{E}_s + \lambda_s\mathrm{tr}(\mathbf{E}_s)\mathbf{I}, \tag{C.4}$$

in which the strain tensor $\mathbf{E}_s = (\nabla\mathbf{u}_s + \nabla\mathbf{u}_s^T)/2$, $\mathbf{u}_s$ being the displacement of the solid phase of the particle. Another consequence of the small-deformation assumption is a small deviation of the fluid and solid volume fractions from their undeformed values. We take the undeformed Darcy particle to be a circle of radius R with uniform porosity $\phi_f|_{t=0} = \phi_0$. Under the small-deformation assumption, the volume fractions ϕ_f and ϕ_s can be taken to be constants in the leading order:

$$\phi_s = \phi_{s0}\hat{J} \approx (1 - \phi_0)(1 - \nabla \cdot \mathbf{u}_s) \approx 1 - \phi_0, \tag{C.5}$$

$$\phi_f \approx \phi_0 + (1 - \phi_0)\nabla \cdot \mathbf{u}_s \approx \phi_0, \tag{C.6}$$

where $\hat{J} = \det(\hat{\mathbf{F}})$ is the determinant of the deformation gradient tensor.

Eliminating $\mathbf{v}_f$ between Eqs. (C.1) and (C.2) yields $\nabla \cdot (\phi_f/\phi_s\nabla p) = 0$. To the leading order, we approximate ϕ_f and ϕ_s by their undeformed constant values, and obtain the Laplace equation for the pressure:

$$\nabla^2 p = 0. \tag{C.7}$$

Eliminating $\mathbf{v}_f$ from Eqs. (C.2) and (C.3), we obtain a relationship between the solid stress and the pressure:

$$\nabla p = \nabla \cdot (\phi_s\boldsymbol{\sigma}_s) \approx (1 - \phi_0)\nabla \cdot \boldsymbol{\sigma}_s, \tag{C.8}$$

where again we make use of $\phi_s \approx 1 - \phi_0$ in the leading order. The two equations above can be recast in terms of the solid stress:

$$\nabla \cdot (\nabla \cdot \boldsymbol{\sigma}_s) = 0, \tag{C.9}$$

$$\nabla \times (\nabla \cdot \boldsymbol{\sigma}_s) = 0. \tag{C.10}$$

Recalling the constitutive equation (C.4), we will solve the above two equations for the solid displacement $\mathbf{u}_s$. Once we have the solid displacement and stress tensor, the fluid velocity $\mathbf{v}_f$ follows from substituting Eq. (C.8) into Eq. (C.2):

$$\mathbf{v}_f = -\frac{1}{\xi}\nabla \cdot \boldsymbol{\sigma}_s. \tag{C.11}$$

We use a polar coordinate system with the origin at the center of the Darcy particle, and $\theta = 0$ along the x-axis of Fig. 12(a). The symmetry of the elongational flow dictates a symmetry in the solid deformation. On the leading order, we postulate a displacement field of the following form:

$$u_{sr}(r, \theta) = f(r) \cdot \cos(2\theta), \quad u_{s\theta} = g(r) \cdot \sin(2\theta). \tag{C.12}$$

Plugging these into the constitutive equation, and then the elastic stress tensor into Eqs. (C.9) and (C.10), we arrive at two ordinary differential equations for $f(r)$ and $g(r)$:

$$-3f - 6g + r[-5f^{(1)} - 2g^{(1)} + r(2f^{(2)} + 2g^{(2)} + rf^{(3)})] = 0, \tag{C.13}$$

$$6f + 3g + 2rf^{(1)} + 5rg^{(1)} - r^2(2f^{(2)} + 2g^{(2)} + rg^{(3)}) = 0, \tag{C.14}$$

where the superscript '(n)' denotes the nth-order derivative. The general solutions of $f(r)$ and $g(r)$ can be written as

$$f(r) = c_1 r + a_3 r^3, \quad g(r) = -c_1 r + b_3 r^3, \tag{C.15}$$

with the coefficients c_1, a_3, b_3 to be determined by the boundary conditions.

C.2. Flow outside the Darcy particle

The flow outside of the Darcy particle is governed by the Stokes equations (Eqs. (1), (2)). Considering the symmetry of the problem and the far-field flow, we postulate a stream function

$$\Psi_e = \left(-\frac{\varepsilon}{2}r^2 + c_2 + d_2 r^{-2}\right) \cdot \sin(2\theta), \tag{C.16}$$

where ε is the constant elongation rate far from the particle, and the c_2 and d_2 terms are the leading-order flow disturbances due to the Darcy particle. Then the velocity and pressure fields can be calculated:

$$V_r = \frac{(-\varepsilon r^4 + 2c_2 r^2 + 2d_2)\cos(2\theta)}{r^3}, \tag{C.17}$$

$$V_\theta = \frac{(2d_2 + \varepsilon r^4)\sin(2\theta)}{r^3}, \tag{C.18}$$

$$P = \frac{4c_2 \mu \cos(2\theta)}{r^2}. \tag{C.19}$$

The coefficients c_2 and d_2 are to be determined, together with c_1, a_3 and b_3, via the boundary conditions on the interface between Darcy particle and the Stokes flow.

C.3. Boundary conditions

We impose Eqs. ((10)–(12)) as boundary conditions on the interface. As noted in Sec. 5.3, the condition on the tangential slip velocity is dropped from BC1 for a Darcy gel. The remaining five scalar BCs are as follows:

$$V_r = \phi_0 v_{fr}, \tag{C.20}$$

$$V_r = \eta(2\mu E_{rr} - P + p), \tag{C.21}$$

$$V_\theta = \beta(2\mu E_{r\theta}), \tag{C.22}$$

$$2\mu E_{rr} - P = (1 - \phi_0)\sigma_{srr} - p, \tag{C.23}$$

$$2\mu E_{r\theta} = (1 - \phi_0)\sigma_{sr\theta}, \tag{C.24}$$

in which E_{rr} and $E_{r\theta}$ are the rr and $r\theta$ components of the strain rate tensor of the exterior fluid, $\mathbf{E} = (\nabla \mathbf{V} + \nabla \mathbf{V}^T)/2$.

By inserting into the above BCs the expressions for the velocity fields $\mathbf{V}$ and $\mathbf{v}_f$, the strain-rate of the external flow $\mathbf{E}$, the pressure fields P and p on either side of the boundary, and the solid stress $\boldsymbol{\sigma}_s$, we obtain five algebraic equations for the constants c_1, a_3, b_3, c_2 and d_2. Upon determining these with the help of symbolic computing, we obtain an approximate solution to the problem. From the displacement field $\mathbf{u}_s = (u_{sr}, u_{s\theta})$, in particular, we can extract the steady-state deformation of the gel particle. In the limit of small deformation, the amount of compression at the equator $u_{sc} = |u_{sr}(R, 0)|$ equals the amount of elongation at the poles $u_{se} = u_{sr}(R, \pi/2)$:

$$u_{se} = \frac{2\varepsilon\mu(A_1 \cdot R^4 + B_1 \cdot R^3 + C_1 \cdot R^2)}{3\mu_s(\lambda_s + \mu_s)(\phi_0 - 1)(A_2 \cdot R^3 + B_2 \cdot R^2 + C_2 \cdot R)}, \tag{C.25}$$

with the following coefficients dependent on the properties of the hydrogel and the fluid:

$$A_1 = 3\eta\lambda_s\xi + 2\eta\mu_s\xi - 3\eta\lambda_s\phi_0\xi - 2\eta\mu_s\phi_0\xi,$$

$$B_1 = 6\lambda_s\phi_0 + 6\mu_s\phi_0 + 12\beta\eta\lambda_s\mu\xi + 12\beta\eta\mu\mu_s\xi - 12\beta\eta\lambda_s\mu\phi_0\xi - 12\beta\eta\mu\mu_s\phi_0\xi,$$

$$C_1 = 24\beta\lambda_s\mu\phi_0 + 36\beta\mu\mu_s\phi_0 + 12\eta\lambda_s\mu\phi_0,$$

$$A_2 = \eta\xi - \eta\phi_0\xi,$$

$$B_2 = 2\phi_0 + 24\beta\eta\mu^2\phi_0 + 4\beta\eta\mu\xi - 4\beta\eta\mu\phi_0\xi,$$

$$C_2 = 8\beta\mu\phi_0 + 8\eta\mu\phi_0.$$

References

[1] J. Jagur-Grodzinski, Polymers for tissue engineering, medical devices, and regenerative medicine. Concise general review of recent studies, Polym. Adv. Technol. 17 (6) (2006) 395–418.
[2] R. Duncan, The dawning era of polymer therapeutics, Nat. Rev. Drug Discov. 2 (5) (2003) 347–360.
[3] F. Fischel-Ghodsian, L. Brown, E. Mathiowitz, D. Brandenburg, R. Langer, Enzymatically controlled drug delivery, Proc. Natl. Acad. Sci. 85 (7) (1988) 2403–2406.
[4] B. Jeong, Y.H. Bae, D.S. Lee, S.W. Kim, Biodegradable block copolymers as injectable drug-delivery systems, Nature 388 (6645) (1997) 860–862.
[5] R. Langer, Drug delivery and targeting, Nature 392 (6679 Suppl) (1998) 5–10.
[6] Y. Luo, M.S. Shoichet, A photolabile hydrogel for guided three-dimensional cell growth and migration, Nat. Mater. 3 (4) (2004) 249–253.
[7] A.P. Nowak, V. Breedveld, L. Pakstis, B. Ozbas, D.J. Pine, D. Pochan, T.J. Deming, Rapidly recovering hydrogel scaffolds from self-assembling diblock copolypeptide amphiphiles, Nature 417 (6887) (2002) 424–428.
[8] D.J. Beebe, J.S. Moore, J.M. Bauer, Q. Yu, R.H. Liu, C. Devadoss, B.-H. Jo, Functional hydrogel structures for autonomous flow control inside microfluidic channels, Nature 404 (6778) (2000) 588–590.
[9] L. Dong, A.K. Agarwal, D.J. Beebe, H. Jiang, Adaptive liquid microlenses activated by stimuli-responsive hydrogels, Nature 442 (7102) (2006) 551–554.
[10] A. Sidorenko, T. Krupenkin, A. Taylor, P. Fratzl, J. Aizenberg, Reversible switching of hydrogel-actuated nanostructures into complex micropatterns, Science 315 (5811) (2007) 487–490.
[11] M.E. Harmon, M. Tang, C.W. Frank, A microfluidic actuator based on thermoresponsive hydrogels, Polymer 44 (16) (2003) 4547–4556.
[12] D. Kim, D.J. Beebe, Hydrogel-based reconfigurable components for microfluidic devices, Lab Chip 7 (2) (2007) 193–198.
[13] D.F. Coutinho, A.F. Ahari, N.N. Kachouie, M.E. Gomes, N.M. Neves, R.L. Reis, A. Khademhosseini, An automated two-phase system for hydrogel microbead production, Biofabrication 4 (3) (2012) 035003.
[14] X. Zhang, L. Li, C. Luo, Gel integration for microfluidic applications, Lab Chip 16 (2016) 1757–1776.
[15] H. Huang, Y. Yu, Y. Hu, X. He, O.B. Usta, M.L. Yarmush, Generation and manipulation of hydrogel microcapsules by droplet-based microfluidics for mammalian cell culture, Lab Chip 17 (11) (2017) 1913–1932.
[16] Š. Selimović, J. Oh, H. Bae, M. Dokmeci, A. Khademhosseini, Microscale strategies for generating cell-encapsulating hydrogels, Polymers 4 (3) (2012) 1554–1579.
[17] W. Hong, X. Zhao, J. Zhou, Z. Suo, A theory of coupled diffusion and large deformation in polymeric gels, J. Mech. Phys. Solids 56 (5) (2008) 1779–1793.
[18] J. Dervaux, M. Ben Amar, Mechanical instabilities of gels, Annu. Rev. Condens. Matter Phys. 3 (2012) 311–332.
[19] M. Bacca, R.M. McMeeking, A viscoelastic constitutive law for hydrogels, Meccanica 52 (2017) 3345–3355.
[20] N. Bouklas, R. Huang, Swelling kinetics of polymer gels: comparison of linear and nonlinear theories, Soft Matter 8 (2012) 8194–8203.
[21] A.D. Drozdov, P. Sommer-Larsen, J. Christiansen, C.-G. Sanporean, Time-dependent response of hydrogels under constrained swelling, J. Appl. Phys. 115 (2014) 233517.
[22] N.J. Balmforth, I.A. Frigaard, G. Ovarlez, Yielding to stress: recent developments in viscoplastic fluid mechanics, Annu. Rev. Fluid Mech. 46 (2014) 121–146.
[23] I.A. Frigaard, Background lectures on ideal visco-plastic fluid flows, in: G. Ovarlez, S. Hormozi (Eds.), Lectures on Visco-Plastic Fluid Mechanics, Springer, 2018, pp. 1–40.
[24] M. Daneshi, Characterising the non-ideal behaviour of a Carbopol gel flowing in thin conduits, PhD thesis, University of British Columbia, Vancouver, Canada, 2020.
[25] M. Moyers-Gonzalez, I.A. Frigaard, Dean flow of a Bingham fluid in a curved rectangular duct, J. Non-Newton. Fluid Mech. 286 (2020) 104440.
[26] A. Wachs, Computational methods for viscoplastic fluid flows, in: G. Ovarlez, S. Hormozi (Eds.), Lectures on Visco-Plastic Fluid Mechanics, Springer, 2018, pp. 83–125.
[27] J.A. Iglesias, G. Mercier, E. Chaparian, I.A. Frigaard, Computing the yield limit in three-dimensional flows of a yield stress fluid about a settling particle, J. Non-Newton. Fluid Mech. 284 (2020) 104374.
[28] C.W. MacMinn, E.R. Dufresne, J.S. Wettlaufer, Large deformations of a soft porous material, Phys. Rev. Appl. 5 (4) (2016) 044020.
[29] M.A. Biot, General theory of three-dimensional consolidation, J. Appl. Phys. 12 (1941) 155–164.
[30] V.C. Mow, S.C. Kuei, W.M. Lai, C.G. Armstrong, Biphasic creep and stress relaxation of articular cartilage in compression: theory and experiments, J. Biomech. Eng. 102 (1980) 73–84.
[31] T.S. Alexiou, G.E. Kapellos, Plane Couette-Poiseuille flow past a homogeneous poroelastic layer, Phys. Fluids 25 (2013) 073605.
[32] M. Minale, Momentum transfer within a porous medium. II. Stress boundary condition, Phys. Fluids 26 (2014) 123102.
[33] H.H. Wei, S.L. Waters, S.Q. Liu, J.B. Grotberg, Flow in a wavy-walled channel lined with a poroelastic layer, J. Fluid Mech. 492 (2003) 23–45.
[34] M. Pourjafar, K. Sadeghy, Pressure-driven flows of Quemada fluids in a channel lined with a poroelastic layer: a linear stability analysis, J. Non-Newton. Fluid Mech. 242 (2017) 23–47.
[35] M. Pourjafar, B. Taghilou, S.M. Taghavi, K. Sadeghy, On the use of biphasic mixture theory for investigating the linear stability of viscous flow through a channel lined with a viscoelastic porous bio-material, Int. J. Non-Linear Mech. 105 (2018) 200–211.
[36] M. Pourjafar, S. Bazargan, K. Sadeghy, Linear stability analysis of time-dependent fluids in plane Couette flow past a poroelastic layer, J. Non-Newton. Fluid Mech. 266 (2019) 1–19.
[37] W. Strychalski, C.A. Copos, O.L. Lewis, R.D. Guy, A poroelastic immersed boundary method with applications to cell biology, J. Comput. Phys. 282 (2015) 77–97.
[38] A. Mogilner, A. Manhart, Intracellular fluid mechanics: coupling cytoplasmic flow and active cytoskeletal gel, Annu. Rev. Fluid Mech. 50 (2018) 347–370.
[39] G.S. Beavers, D.D. Joseph, Boundary conditions at a naturally permeable wall, J. Fluid Mech. 30 (1967) 197–207.
[40] B. Alazmi, K. Vafai, Analysis of fluid flow and heat transfer interfacial conditions between a porous medium and a fluid layer, Int. J. Heat Mass Transf. 44 (2001) 1735–1749.

[41] Y.-N. Young, Y. Mori, M.J. Miksis, Slightly deformable Darcy drop in linear flows, Phys. Rev. Fluids 4 (6) (2019) 063601.
[42] J.J. Feng, Y.-N. Young, Boundary conditions at a gel-fluid interface, Phys. Rev. Fluids 5 (Dec. 2020) 124304.
[43] J.A. Ochoa-Tapia, S. Whitaker, Momentum transfer at the boundary between a porous medium and a homogeneous fluid - I. Theoretical development, Int. J. Heat Mass Transf. 38 (14) (1995) 2635–2646.
[44] J.A. Ochoa-Tapia, S. Whitaker, Momentum transfer at the boundary between a porous medium and a homogeneous fluid - II. Comparison with experiment, Int. J. Heat Mass Transf. 38 (1995) 2647–2655.
[45] M.L. Bars, M.G. Worster, Interfacial conditions between a pure fluid and a porous medium: implications for binary alloy solidification, J. Fluid Mech. 550 (2006) 149–173.
[46] Y. Mori, H. Chen, C. Micek, M.-C. Calderer, A dynamic model of polyelectrolyte gels, SIAM J. Appl. Math. 73 (1) (2013) 104–133.
[47] J. Shen, X. Yang, Numerical approximations of Allen-Cahn and Cahn-Hilliard equations, Discrete Contin. Dyn. Syst. 28 (4) (2010) 1669–1691.
[48] T. Richter, Fluid-Structure Interactions: Models, Analysis and Finite Elements, Springer, 2017.
[49] D. Arndt, W. Bangerth, B. Blais, T.C. Clevenger, M. Fehling, A.V. Grayver, T. Heister, L. Heltai, M. Kronbichler, M. Maier, et al., The deal.II library, version 9.2, J. Numer. Math. 28 (3) (2020) 131–146.
[50] T.A. Davis, Algorithm 832: UMFPACK v4.3—an unsymmetric-pattern multifrontal method, ACM Trans. Math. Softw. 30 (June 2004) 196–199.
[51] J.D. Sherwood, Tip streaming from slender drops in a nonlinear extensional flow, J. Fluid Mech. 144 (1984) 281–295.
[52] R. Suryo, O.A. Basaran, Tip streaming from a liquid drop forming from a tube in a co-flowing outer fluid, Phys. Fluids 18 (8) (2006) 082102.